Theoretical Study of the Oxidation Mechanisms of Naphthalene Initiated by Hydroxyl Radicals: The OH–Addition Pathway

3 AUTHORS:

Abolfazl Shiroudi
Hasselt University
39 PUBLICATIONS **65** CITATIONS

SEE PROFILE

Michael S Deleuze
Hasselt University
132 PUBLICATIONS **2,673** CITATIONS

SEE PROFILE

Sebastien Canneaux
Université des Sciences et Technologies de Lill…
31 PUBLICATIONS **248** CITATIONS

SEE PROFILE

Theoretical Study of the Oxidation Mechanisms of Naphthalene Initiated by Hydroxyl Radicals: The OH-Addition Pathway

Abolfazl Shiroudi,[†] Michael S. Deleuze,*[,†] and Sébastien Canneaux[‡]

[†]Center of Molecular and Materials Modelling, Hasselt University, Agoralaan, Gebouw D, B-3590 Diepenbeek, Belgium
[‡]Université Lille1 Sciences et Technologies, Cité scientifique, 59655 Villeneuve d'Ascq Cedex, France

S *Supporting Information*

ABSTRACT: The oxidation mechanisms of naphthalene by OH radicals under inert (He) conditions have been studied using density functional theory along with various exchange–correlation functionals. Comparison has been made with benchmark CBS-QB3 theoretical results. Kinetic rate constants were correspondingly estimated by means of transition state theory and statistical Rice–Ramsperger–Kassel–Marcus (RRKM) theory. Comparison with experiment confirms that, on the OH-addition reaction pathway leading to 1-naphthol, the first bimolecular reaction step has an effective negative activation energy around -1.5 kcal mol^{-1}, whereas this step is characterized by an activation energy around 1 kcal mol^{-1} on the OH-addition reaction pathway leading to 2-naphthol. Effective rate constants have been calculated according to a steady state analysis upon a two-step model reaction mechanism. In line with experiment, the correspondingly obtained branching ratios indicate that, at temperatures lower than 410 K, the most abundant product resulting from the oxidation of naphthalene by OH radicals must be 1-naphthol. The regioselectivity of the OH$^{•}$-addition onto naphthalene decreases with increasing temperatures and decreasing pressures. Because of slightly positive or even negative activation energies, the RRKM calculations demonstrate that the transition state approximation breaks down at ambient pressure (1 bar) for the first bimolecular reaction steps. Overwhelmingly high pressures, larger than 10^5 bar, would be required for restoring to some extent (within ~5% accuracy) the validity of this approximation for all the reaction channels that are involved in the OH-addition pathway. Analysis of the computed structures, bond orders, and free energy profiles demonstrate that all reaction steps involved in the oxidation of naphthalene by OH radicals satisfy Leffler–Hammond's principle. Nucleus independent chemical shift indices and natural bond orbital analysis also show that the computed activation and reaction energies are largely dictated by alterations of aromaticity, and, to a lesser extent, by anomeric and hyperconjugative effects.
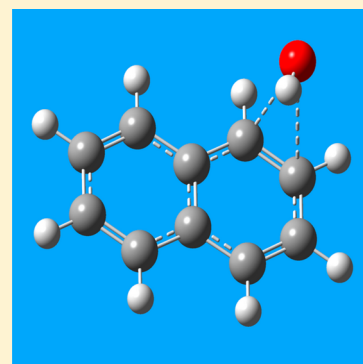
1. INTRODUCTION

Polycyclic aromatic hydrocarbons (PAHs) are ubiquitous environmental pollutants. Many PAHs are potentially genotoxic, mutagenic, or carcinogenic.[1,2] They are emitted into the atmosphere during incomplete combustion of a variety of sources such as fossil fuels and biomass.[3–5] PAHs are chemically reactive to tropospheric gases such as ozone, nitrate radicals, and hydroxyl radicals. The most important sink reactions of organic compounds in the troposphere are the reactions with OH radicals,[6,7] which play a key role in determining the oxidation power of the atmosphere.[8] Under ambient conditions, the oxidation of aromatic rings by OH radicals in the gas phase yields hydroxycyclohexadienyl-type radicals, which can back-decompose to the reactants or react with NO_2 or O_2 to yield further strongly mutagenic derivatives.[9–14] Naphthalene is the most abundant PAH in polluted urban areas and is reactive in ambient atmospheres.[15,16] Reactions of naphthalene in the atmosphere often yield degradation products that may be more carcinogenic than the parent PAH.[17] Therefore, it is of utmost importance to understand the degradation mechanisms of naphthalene in the presence of oxidant species.

Lorenz and Zellner[14,18] as well as Atkinson and co-workers[19–21] have experimentally studied the gas phase reaction between hydroxyl radicals and naphthalene at temperatures lower than 410 K and at temperatures ranging from 636 to 873 K, by means of laser flash photolysis using laser-induced fluorescence, at pressures between 6 and 128 mbar, under inert (He) conditions.[9,14] An Arrhenius plot of all the kinetic rate constants that were measured or experimentally inferred so far under such conditions[22] is depicted in Figure 1.

As is quite apparent from this figure, different energy barriers prevail at temperatures lower than 410 K and at temperatures higher than 636 K. To explain such features, two different pathways have been suggested[8] for the reaction between naphthalene and OH radicals in the gas phase.

At low temperatures (at $T \leq 410$ K), an OH-addition process, involving first an attack of OH radicals on naphthalene at the C_1 and C_2 positions (Figure 2), followed by hydrogen elimination, is assumed to prevail, whereas at high temperatures
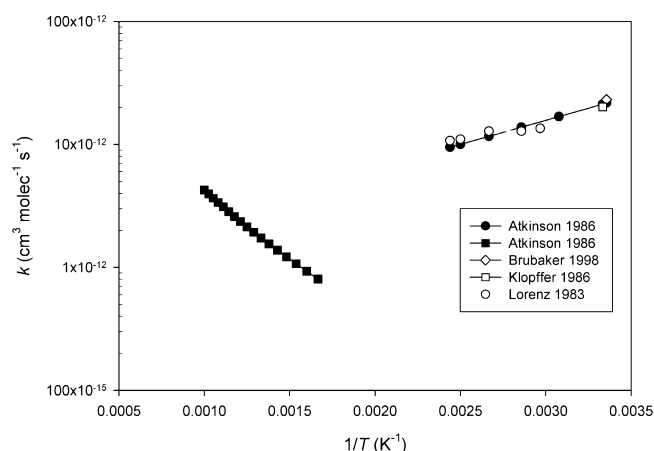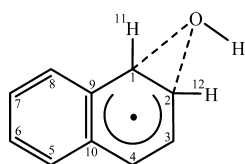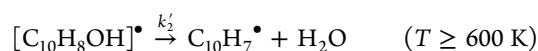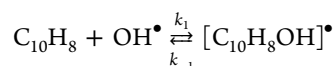
Figure 1. Arrhenius plot of the rate constants for the reaction of OH radicals with naphthalene: Legend: (●) Atkinson et al.;[19] (■) Atkinson et al.;[21] (◇) Brubaker and Hites;[23] (□) Klöpffer et al.;[24] (○) Lorenz and Zellner.[14]

Figure 2. Retained atom labeling for characterizing the structures of intermediate and transition states during the oxidation of naphthalene by OH radicals (see Tables 1 and 2 for numerical details).

(at $T \geq 600$ K), the mechanism which is believed to dominate is an OH-addition process, via attack of OH radicals on the hydrogen atoms linked to the C_1 and C_2 atoms, followed by water elimination. These low and high temperature pathways are commonly referred to as the hydroxyl radical addition and hydrogen abstraction pathways, respectively.

$$C_{10}H_8 + OH^\bullet \underset{k_{-1}}{\overset{k_1}{\rightleftharpoons}} [C_{10}H_8OH]^\bullet$$

$$[C_{10}H_8OH]^\bullet \overset{k_2}{\to} C_{10}H_7OH + H^\bullet \qquad (T \leq 410 \text{ K})$$

$$[C_{10}H_8OH]^\bullet \overset{k_2'}{\to} C_{10}H_7^\bullet + H_2O \qquad (T \geq 600 \text{ K})$$

As is immediately apparent from Figure 1, the rate constant of the reaction between OH radicals and naphthalene at $T \leq 410$ K exhibits[14,19−21] a negative temperature dependence, which is equivalent to an Arrhenius activation energy of -1.27[18,19] or -1.8 kcal mol^{-1}.[25] A least-squares fit of experimental rate constants yields accordingly the following Arrhenius expression:[25]

$$k_{(T \leq 410K)} = (1.335 \pm 0.825) \times 10^{-12} e^{(902 \pm 240)/T}$$

$$\text{cm}^3 \text{ molecule}^{-1} \text{ s}^{-1}$$

The above Arrhenius rate constant decreases with increasing temperature at pressures between 6 and 128 mbar (He). The corresponding values vary from $(18.6 \pm 1.0) \times 10^{-12}$ to $(10.5 \pm 4.0) \times 10^{-12}$ cm^3 molecule^{-1} s^{-1} over the temperature range 300−407 K.

Under atmospheric conditions, attack of OH radicals on naphthalene is initiated by addition at the C_1 and C_2 positions (Figure 3) to give the adducts **I** and **II** (Scheme 1).[14,19,20] In line with the assumption of a first reversible addition step, the
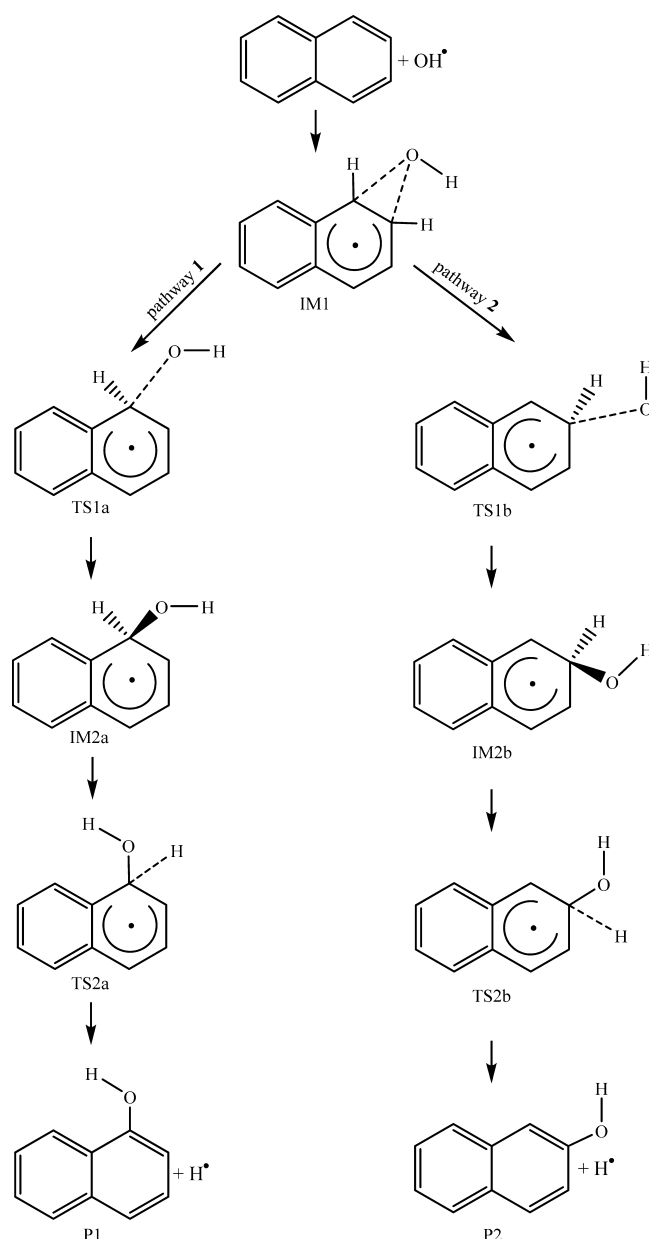
Figure 3. Reaction pathways for the oxidation of naphthalene by hydroxyl radicals into 1-naphthol (P1) and 2-naphthol (P2).

Scheme 1
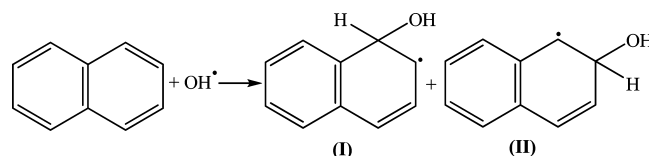
negative or slightly positive activation energies of these reactions indicates that a major reaction channel of these adducts is loss of hydroxyl radicals to regenerate reactants.[6] Upon investigating the regioselectivity of the OH-addition reactions on naphthalene under inert (He) atmosphere, Bernstein and co-workers experimentally observed that the production of 1-hydroxynaphthalene (or 1-naphthol) was favored by a ratio 2:1 over 2-hydroxynaphthalene (or 2-naphthol), according to a personal communication to Ricca and Bauschlicher.[26]

The interactions between naphthalene and hydroxyl radical at total pressures between 6 and 128 mbar (He) were found to be essentially pressure independent.[14] This is only at pressures smaller than 10 mbar that a slight decrease of the rate constants measured at 379 K has been observed.[14] Rate constants at 525 K show no pressure effects but are lower in absolute magnitude by almost an order of magnitude. This behavior was interpreted[14] as to arise from an addition reaction at lower temperatures and from its reversibility at higher temperatures.

These addition reactions have been the subject of a few theoretical studies, comprising the investigations at the B3LYP/6-31G* level of theory by Ricca and Bauschlicher[26] and at the BB1K/6-311+G(3df,2p)//BB1K/6-31+G(d,p) level of theory by Qu et al.[8] More recently, Zhang et al.[27] found that the initial OH-addition reactions upon naphthalene at the C_1 and C_2 positions (Figure 3) are characterized by negative energy barriers of -3.42 and -2.22 kcal mol^{-1}, respectively, at the B3LYP/6-311+G(2df,p) level of theory, whereas positive energy barriers of 0.41 and 1.65 kcal mol^{-1} were correspondingly obtained at the BB1K/6-311++G(2df,2p) level of theory.

The main purpose of our work is to reinvestigate the OH-addition pathway through a detailed analysis of the kinetic rate constants obtained in the experimental study by Lorenz and Zellner[14] of the reaction of naphthalene by hydroxyl radicals under inert conditions, i.e., using He as diluent gas, and thus, in the absence of O_2. For this purpose, we will study the two reaction pathways **1** and **2** that are depicted in Figure 3 by means of density functional theory (DFT), along with various exchange−correlation functionals. These pathways are initiated by OH-addition on naphthalene at the C_1 and C_2 positions (Figure 2), which leads to 1-naphthol and 2-naphthol, respectively.

The addition of the hydroxyl radical to naphthalene starts with the formation of a prereactive molecular complex, IM1 (Figure 3). The reaction proceeds in two steps, involving first a fast and reversible reaction between the OH radical and naphthalene to form an energized adduct $[C_{10}H_8OH]^\bullet$ (IM2), followed by an irreversible step, corresponding to the unimolecular dissociation of this adduct into 1- or 2-naphthol and one H atom (H$^\bullet$). We note here that the likelihood of the hydroxyl radical addition pathway under inert conditions has been discussed in the past by Hollman et al. in the frame of a theoretical study of the oxidation mechanisms of benzene by hydroxyl radicals.[28] Benzene, however, is much less reactive than naphthalene, and conclusions drawn from calculations on the former compound are not necessarily transposable to the latter one. Indeed, as n-acene length increases, their reactivity generally increases.[29] Such progressions in n-acene properties appear to coincide with the sequential loss of benzenoid character (aromaticity) predicted by early molecular orbital treatments and Clar's qualitative sextet concept.[30]

For the sake of quantitative insights into these reaction mechanisms, comparison will be made with benchmark theoretical calculations employing the high-level composite CBS-QB3 ab initio approach,[31−39] to determine which exchange−correlation functional gives the most accurate energy barriers and reaction energies. We note that DFT methods alone were found to be insufficient for quantitatively investigating the potential energy surface associated with the OH-addition reactions upon benzene.[28] With the CBS-QB3 approach, an extrapolation scheme is used to evaluate SCF and correlation energies in the limit of a complete basis set (CBS). The obtained results are analyzed in terms of nucleus independent chemical shift (NICS) indices of aromaticity,[40−44] bond orders, natural bond orbital (NBO) occupancies,[45,46] and donor−acceptor interaction energies.

2. COMPUTATIONAL DETAILS

All calculations that are discussed in the present work have been performed using the Gaussian 09 package of programs[47] at the Flemish Supercomputer Center. Molecular structures were visualized with GaussView.[48] The most accurate of these calculations were conducted at the CBS-QB3 level of theory.[31−39] This composite method belongs to the family of the complete basis set methods of Petersson and co-workers,[37] which were developed with the idea that a major source of error in quantum mechanical calculations arises from truncation of the basis set. The CBS models extrapolate to the CBS limit by using N^{-1} asymptotic convergence of MP2 pair energies calculated from pair natural orbital expansions. CBS models involve low-level (SCF and ZPE) calculations on large basis sets, midsized basis sets for second-order correlation corrections, and small basis sets for high-level correlation corrections. They include an extrapolation of energies up to the CCSD(T) level (coupled cluster theory along with single, double and perturbative triple electronic excitations[49−51]) in the limit of a complete basis set to correct Møller−Plesset second-order (MP2) energies.[52] In addition, this approach includes empirical corrections for spin contamination. The CBS-QB3 method involves five steps, starting with a geometry optimization at the B3LYP level of theory,[53,54] followed by a calculation of vibrational frequencies and canonical partition functions to obtain thermal corrections to enthalpies, zero-point vibrational energies, and entropies.[55] Specifically, the CBS-QB3 method involves the following steps:[31]

- B3LYP/6-311G(2d,d,p) geometry optimization
- B3LYP/6-311G(2d,d,p) frequency calculation with a 0.99 scale factor for the ZPE
- CCSD(T)/6-31+G* energy calculation
- MP4(SDQ)/6-31+G(d(f),p) energy calculation
- UMP2/6-311+G(3d2f,2df,2p) energy calculation and CBS extrapolation

The CBS-QB3 approach is known to yield mean absolute deviation of only 1.1 kcal mol^{-1} on the G2/97 test set[39] for reaction energies, which can hardly be surpassed by any other method these days. A more recent work indicates a maximum error of 2.8 kcal mol^{-1} for the G2 test set of reaction energies, and average and mean absolute errors of 0.2 and 0.98 kcal mol^{-1},[56] which at first glance seems amply sufficient for our purposes. In addition, we note that the CBS-QB3 approach includes a correction for spin contamination in open-shell species.[32−38]

DFT calculations, comprising geometry optimizations and frequency calculations, were performed using a variety of exchange−correlation functionals, such as the Becke-3-parameter-Lee−Yang−Parr (B3LYP) functional,[53,54] the dispersion corrected ωB97XD exchange−correlation functional,[57] and the UM05-2x[58] and UM06-2x functionals[58] in conjunction with the augmented correlation consistent aug-cc-pVTZ basis set.[59] Thermodynamic state functions were correspondingly computed from canonical partition functions for an ideal gas, using Boltzmann statistical thermodynamics along with the rigid rotor-harmonic oscillator approximation (RRHO),[60,61] and neglecting thereby hindered rotations of the OH group in the intermediates and transition states. We note that, upon considering the results of a systematic study of the thermochemical properties of ten target species involved in the oxidation of o-xylene, it is reasonable to assume that internal rotations need only to be accounted for at temperatures larger than 400 K.[62]

The intrinsic reaction coordinate (IRC) path[63] was traced at the B3LYP/6-31G(d,p) level of theory to check the energy profiles connecting each transition structure to the two associated minima of the proposed mechanism by using the second-order Gonzalez–Schlegel integration method.[63,64] Energy barriers obtained on DFT grounds were systematically corrected for basis set superposition errors (BSSEs),[65] according to the counterpoise method proposed by Boys and Bernardi.[66] In this *a posteriori* correction method, the energy calculations for the individual monomers are performed using the whole supermolecular basis sets instead of the monomer basis sets. No symmetry constraints were imposed during the geometry optimizations.[67,68] The keyword *nosymm* was used to guarantee this matter.

The rate constants and the branching ratios for each reaction channels were evaluated using transition state theory (TST) at a pressure of 1 bar, and at temperatures ranging from 300 to 407 K, using the CBS-QB3 estimates for activation energies, and B3LYP/6-311G(2d,d,p) partition functions. In atmospheric chemistry, the kinetics of bimolecular and unimolecular reactions can be determined using conventional transition state theory. The rate constants for these reactions are therefore given by[69–71]

$$k_{\text{TST}} = \kappa(T) \frac{\sigma k_{\text{B}} T}{h} V_{\text{m}}(T) \frac{Q_{\text{TS}}^{\ddagger}(T)}{Q_{\text{A}}(T) \cdot Q_{\text{B}}(T)} \exp(-E_{\text{a}}/RT)$$

(for bimolecular reactions)   (1)

$$k_{\text{TST}} = \kappa(T) \frac{\sigma k_{\text{B}} T}{h} \frac{Q_{\text{TS}}^{\ddagger}(T)}{Q_{\text{A}}(T)} \exp(-E_{\text{a}}/RT)$$

(for unimolecular reactions)   (2)

along with $\kappa(T)$, a relevant tunneling correction factor. Because the moving entity at the transition state involves a relatively heavy oxygen atom, this factor has been assumed to be equal to 1 for the first bimolecular OH-addition step. On the other hand, in view of a strongly asymmetric energy barrier, and because the moving entity corresponds to a hydrogen atom, an Eckart tunneling correction factor[72] has been considered for evaluating the rate constant of the unimolecular dissociation step (step 2) on TST grounds, using the CBS-QB3 energy profiles (these factors range from 1.5 to 2.4, see Table S1 of the Supporting Information for details).

Equation 1 applies to the first bimolecular reaction step (R → IM2a or IM2b), whereas eq 2 applies to all other reaction steps that are depicted in Figure 3. Note that eq 1 derives from a steady state analysis involving a reversible reaction, followed by an irreversible step (R ⇄ IM1 → IM2x, with x = a, b), upon considering that $k_{\text{IM1}\rightarrow\text{IM2a}}$ or $k_{\text{IM1}\rightarrow\text{IM2b}}$ are much (at least 10^4 times) smaller than $k_{\text{IM1}\rightarrow\text{R}}$—an assumption in line with detailed theoretical estimates of unimolecular reaction rate constants (see further discussion).

In the above equations, σ denotes the reaction symmetry number, $Q_{\text{TS}}^{\ddagger}$ is the total partition function of the transition state, Q_{A} and Q_{B} represent the total partition functions of the reactants, E_{a} is the classical barrier height (including zero-point vibrational energy contributions), R is the ideal gas constant, k_{B} and h are the Boltzmann's and Planck's constants, respectively, and $V_{\text{m}}(T) = RT/P$ is the molar volume of an ideal gas at the considered temperatures. Because the computed energy differences account for zero-point vibrational energies, vibrational

partition functions were computed using the vibrational ground state as energy reference. TST gives an estimate of the upper-limit for rate constants as a function of the temperature and is known to give reliable estimations of rate constants[73,74] in the high pressure limit,[75] especially for cases with significant barrier heights.[76]

Furthermore, in the present study, statistical Rice–Ramsperger–Kassel–Marcus (RRKM) theory[77–79] has been considered to evaluate pressure effects on a microcanonical basis, both in the falloff regime and toward the high pressure limit, using the implementation of this approach in the Kinetic and Statistical Thermodynamic Package (KiSThelP).[80] As shall be seen, ambient pressure may not necessarily be sufficient to warrantee that the TST approximation is necessarily valid. Again, in these RRKM calculations, a scaling factor of 0.99 was imposed on the frequencies calculated at the B3LYP/6-311G(2d,d,p) level of theory. Collisional stabilization rate constants were computed using Lennard-Jones collision rate theory.[81] The strong collision approximation is used, assuming therefore that every collision deactivates with $\omega = \beta_{\text{c}} Z_{\text{LJ}} [\text{M}]$ being the effective collision frequency, where β_{c} is the collisional efficiency, Z_{LJ} is the Lennard-Jones collision frequency, and $[\text{M}]$ is the total gas concentration. The retained value for β_{c} is 0.2. The collision frequencies (Z_{LJ}) were calculated using the Lennard-Jones parameters: ε/k_{B}, which depends on the energy depth (ε) of the Lennard-Jones potential, and σ, which represents a dimensional scale of the molecular radius.[80] The Lennard-Jones potential parameters for helium as diluent gas[82] amount to σ = 2.28 Å and ε/k_{B} = 10.2 K. For naphthalene and the naphthol radicals, the following parameters have been retained: σ = 6.45 Å, ε/k_{B} = 554.4 K;[83] and σ = 6.57 Å, ε/k_{B} = 612.7 K,[83] respectively.

Assuming again a steady state regime, the rate constants k for the bimolecular reactions leading to the energized adducts (R → IM2x, x = a, b) were calculated according to the scheme advocated by Singleton and Cvetanovic[84] for prereactive complexes. We assume therefore that these bimolecular reactions occur according to a mechanism involving first a fast pre-equilibrium (K_{c}) between the reactants and the prereactive van der Waals complex (IM1), followed by an irreversible step corresponding to the formation of a covalent bond between the OH radical and naphthalene, which leads to the postreactive complexes IM2a or IM2b. Upon using this scheme, the rate constants for the bimolecular reactions (step 1) yielding IM2a or IM2b can be obtained by means of

$$k_{\text{R}\rightarrow\text{IM2x}} = \frac{k_{\text{IM1}\rightarrow\text{R}} \times K_{\text{c}} \times k_{\text{IM1}\rightarrow\text{IM2x}}}{k_{\text{IM1}\rightarrow\text{R}} + k_{\text{IM1}\rightarrow\text{IM2x}}}$$

(3)

where $k_{\text{IM1}\rightarrow\text{R}}$ and $k_{\text{IM1}\rightarrow\text{IM2x}}$ represent reverse and forward unimolecular reaction rate constants (in s^{-1}).

3. RESULTS AND DISCUSSION

3.1. Geometry Optimizations. The optimized molecular structures of the intermediate complexes (IM1 and IM2), transition states (TS1 and TS2), and products (P1 and P2) in the reactions between naphthalene and OH radicals along pathways **1–2** are presented in Tables 1 and 2, according to the atom labels given in Figure 2. In line with changes in chemical bond orders, examination of Tables 1 and 2 and comparison of the structures for the intermediates IM1 and IM2a (IM2b) show that addition of an hydroxyl radical at position C_1 (C_2) results in a significant lengthening of the chemical bonds C_1–C_2 and C_1–C_9 (C_1–C_3). For both chemical pathways (**1 and 2**), it

appears that the corresponding transition state (TS1a or TS1b) is structurally much closer to the prereactive intermediate (IM1) than the produced energized adducts (IM2a or IM2b). The C_2−O forming bond is slightly shorter by ∼0.05 to ∼0.15 Å, in the TS1b transition structure on pathway 2 than in the TS1a transition structure on pathway 1 (Figure 3).

In the next step, from the energized adducts (IM2a and IM2b) to the naphthol products (P1 and P2), the elimination of the hydrogen atom allows IM2a and IM2b to return to an aromatic system. Therefore, also in line with changes in chemical bond orders, the departure of one hydrogen atom (H_{11} or H_{12}) results in a significant shortening of the chemical bonds C_1−C_2 and C_1−C_9 (C_1−C_3). In this case, the corresponding transition states are structurally much closer to the products.

Prior to ending this discussion of geometric parameters, it is worth noticing that, at the starting B3LYP/6-311G(2d,d,p) level of theory used to optimize the geometries of reactants, transition states, and adducts, the spin contamination $[\langle S^2 \rangle_{obs} - 0.75]$ never exceeds 0.034 (Table S2 of the Supporting Information) and can thus, for all practical purposes, be regarded as negligible.

3.2. Energetic and Thermodynamic Parameters. The reader is referred to Tables 3 and 4, for the total internal energies (comprising BSSE and ZPVE corrections) at 0 K and enthalpies and Gibb's free energies at 298 K of all identified transition states and intermediates along pathways 1 and 2 relative to the reactants. In line with experimental Arrhenius activation energies of −1.27[18,19] or −1.8 kcal mol^{-1},[25] all our calculations locate the transition state TS1a on pathway 1 at 0.6−3.9 kcal mol^{-1} below the reactants. Our best (CBS-QB3) estimated value for the corresponding activation energy amounts to −1.5 kcal mol^{-1}. On the other hand, at this level, the transition state TS1b on pathway 2 is located at 1 kcal mol^{-1} above the reactants. According to Ricca and Bauschlischer,[26] this difference in activation energies for the bimolecular reactions R → IM2a and R → IM2b explains that the production of 1-naphthol is kinetically favored over 2-naphthol. However, the subsequent unimolecular dissociation reaction steps IM2a → P1 and IM2b → P2 are characterized by much higher activation energies (Figures 4 and 5). In the high pressure limit, and in the absence of O_2 (as was the case in the original experiment by Lorenz and Zellner[14]), these unimolecular reaction steps may also strongly influence the overall reaction dynamics—an observation that justifies the forthcoming discussion of TST and RRKM kinetic rate constants.

As can be seen in Tables 3 and 4, the newly supplied CBS-QB3 data differ sensitively from those reported by Ricca and Bauschlicher[26] or by Zhang et al.[27] Among all supplied data, energy values obtained with the UM05-2x functional appear on average to be in closest agreement with the benchmark CBS-QB3 results. From the data supplied in Table 4, we characterize in detail (Table 5) the energy barriers associated with the conversion of the prereactive intermediate IM1 into the energized adduct IM2 and with the conversion of the latter into the naphthol products (see also Figures 4 and 5). The CBS-QB3 results show that the first energy barriers (IM1 → TS1) encountered along the chemical reaction pathways 1 and 2 amount to 0.9 and 3.5 kcal mol^{-1}, respectively. TS1a and TS1b are characterized by NICS indices equal to −15.43 and −13.56, respectively. Evidently, the more pronounced aromatic nature of TS1a explains its higher stability, compared with that of TS1b. Also, the lower energy of IM2a compared with that for IM2b reflects the more strongly pronounced aromatic nature of the former energized adduct: indeed, IM2a and IM2b are

Table 1. Main Structural Parameters for All Stationary Points Involved in the Chemical Reaction Pathway 1 (Figure 3) for the Oxidation of Naphthalene by OH• into 1-Naphthol (Atom Labeling in Figure 2)[a]

parameter	B3LYP/aug-cc-pVTZ					ωB97XD/aug-cc-pVTZ					UM05-2x/aug-cc-pVTZ					UM06-2x/aug-cc-pVTZ					B3LYP/6-311G(2d,d,p)				
	IM1	TS1a	IM2a	TS2a	P1	IM1	TS1a	IM2a	TS2a	P1	IM1	TS1a	IM2a	TS2a	P1	IM1	TS1a	IM2a	TS2a	P1	IM1	TS1a	IM2a	TS2a	P1
$r(C_1-C_2)$	1.384	1.391	1.495	1.395	1.373	1.371	1.385	1.494	1.390	1.368	1.385	1.427	1.491	1.387	1.366	1.367	1.388	1.494	1.391	1.368	1.384	1.395	1.500	1.400	1.377
$r(C_1-C_9)$	1.422	1.428	1.517	1.439	1.425	1.419	1.428	1.514	1.437	1.424	1.415	1.427	1.509	1.433	1.421	1.417	1.430	1.513	1.439	1.424	1.424	1.433	1.516	1.443	1.429
$r(C_2-C_3)$	1.408	1.404	1.367	1.400	1.406	1.411	1.403	1.363	1.400	1.405	1.412	1.403	1.363	1.400	1.405	1.414	1.405	1.363	1.401	1.407	1.414	1.407	1.369	1.403	1.409
$r(C_9-C_{10})$	1.426	1.424	1.415	1.424	1.430	1.416	1.414	1.407	1.414	1.420	1.411	1.411	1.404	1.412	1.418	1.418	1.414	1.408	1.414	1.421	1.430	1.428	1.418	1.427	1.433
$r(C_1-H_{11})$	1.079	1.078	1.096	1.832		1.081	1.079	1.095	1.823		1.076	1.076	1.092	1.814		1.082	1.080	1.096	1.749		1.081	1.080	1.105	1.830	
$r(C_1-O)$	2.372	2.190	1.448	1.369	1.366	2.535	2.154	1.431	1.359	1.357	2.679	2.112	1.436	1.364	1.362	2.907	2.091	1.429	1.364	1.359	2.439	2.156	1.445	1.368	1.366
$\angle H_{11}-C_1-O$	79.3	81.3	102.2	97.9		84.4	83.6	103.0	98.8		90.2	84.7	103.1	98.6		101.3	84.8	103.0	99.1		79.4	82.4	107.6	98.1	

[a]Bond lengths are given in angstroms (Å), and bond angles are given in degrees.

4597

dx.doi.org/10.1021/jp411327e | J. Phys. Chem. A 2014, 118, 4593−4610

Table 2. Main Structural Parameters for All Stationary Points Involved in the Chemical Reaction Pathway 2 (Figure 3) for the Oxidation of Naphthalene by OH• into 2-Naphthol (Atom Labeling in Figure 2)[a]

parameter	B3LYP/aug-cc-pVTZ					ωB97XD/aug-cc-pVTZ					UM05-2x/aug-cc-pVTZ					UM06-2x/aug-cc-pVTZ					B3LYP/6-311G(2d,d,p)				
	IM1	TS1b	IM2b	TS2b	P2	IM1	TS1b	IM2b	TS2b	P2	IM1	TS1b	IM2b	TS2b	P2	IM1	TS1b	IM2b	TS2b	P2	IM1	TS1b	IM2b	TS2b	P2
$r(C_1-C_2)$	1.384	1.396	1.492	1.395	1.372	1.371	1.388	1.491	1.387	1.366	1.368	1.387	1.488	1.387	1.365	1.367	1.389	1.491	1.390	1.367	1.384	1.399	1.496	1.399	1.376
$r(C_1-C_9)$	1.422	1.411	1.393	1.410	1.416	1.419	1.412	1.392	1.407	1.415	1.415	1.410	1.392	1.410	1.413	1.417	1.412	1.396	1.409	1.415	1.424	1.415	1.397	1.413	1.419
$r(C_2-C_3)$	1.408	1.430	1.495	1.432	1.413	1.411	1.428	1.494	1.429	1.412	1.412	1.427	1.493	1.429	1.411	1.414	1.430	1.496	1.434	1.414	1.414	1.433	1.499	1.436	1.417
$r(C_3-C_4)$	1.372	1.360	1.338	1.359	1.367	1.364	1.355	1.332	1.353	1.361	1.364	1.355	1.331	1.353	1.361	1.367	1.356	1.333	1.354	1.362	1.374	1.364	1.341	1.362	1.369
$r(C_2-H_{12})$	1.080	1.078	1.102	1.774		1.080	1.078	1.102	1.754		1.078	1.075	1.097	1.754		1.081	1.078	1.102	1.702		1.082	1.080	1.106	1.772	
$r(C_2-O)$	2.672	2.070	1.454	1.372	1.368	2.678	2.065	1.435	1.367	1.359	2.732	2.057	1.442	1.367	1.364	2.932	2.043	1.434	1.367	1.361	2.637	2.056	1.450	1.370	1.366
$\angle H_{12}-C_2-O$	88.8	83.7	106.9	97.3		89.3	85.2	107.7	97.7		92.2	85.6	107.4	97.7		102.2	85.7	107.6	97.8		85.9	84.8	107.5	97.7	

[a]Bond lengths are given in angstroms (Å), and bond angles are given in degrees.

characterized by NICS indices equal to −3.94 and −1.28, respectively.

In Table 5, we provide reaction energies, enthalpies, entropies and Gibb's free energies for the conversion of naphthalene and OH radical (the reactants, R) into 1- and 2-naphthol plus one hydrogen atom (the products, P). Pathway 1 (R → P1) is an endothermic process ($\Delta H = 1$ kcal mol^{-1}), whereas pathway 2 (R → P2) is slightly exothermic ($\Delta H = -0.1$ kcal mol^{-1}). Both pathways are found to be endergonic processes ($\Delta G > 0$) at ambient temperature and pressure. On both pathways (Figures 4 and 5), the global energy minima correspond to the energized adducts, IM2a and IM2b. At the benchmark CBS-QB3 level of theory, these are found to lie at 22.9 and 18.4 kcal mol^{-1}, respectively, below the reactants (Table 4). These stabilization energies are rather close to the BB1K/6-31+G(d,p) values (21.19 and 16.34 kcal mol^{-1}) supplied in the last theoretical study by Qu et al.[8] The highest energies on both pathways correspond to the second transition states (TS2) describing the unimolecular dissociation of the energized adduct into 1- or 2-naphthol and one H atom. Our calculations show that, for the hydrogen elimination from the C_1 and C_2 positions, the corresponding transition states (TS2a and TS2b) lie 6.5 and 9.8 kcal mol^{-1}, respectively, above the reactants (Figures 4 and 5). The barrier heights for the IM2a → P1 and IM2b → P2 decomposition reactions amount to 29.4 and 28.2 kcal mol^{-1}, respectively (Table 3).

As was to be expected, DFT calculations in conjunction with the B3LYP functional underestimate the reaction barriers, due to the self-interaction error. We also note that, in line with observations made in recent works,[85,86] excluding the BSSE from UM05-2x and UM06-2x energy barriers would slightly improve the agreement with the benchmark and BSSE-free CBS-QB3 results, presumably because of a fortuitous cancellation of further errors (basis set convergence error versus the approximate treatment of electron correlation and neglect of spin−orbit interactions). This observation seems to confirm the superiority of the latter two functionals for chemical kinetics. Nevertheless, some care is needed, because the UM05-2x and UM06-2x functionals do not incorporate corrections for dispersion forces, such as the ωB97XD functional. The computed BSSE corrections are around 0.2 kcal mol^{-1} whereas the differences between the B3LYP and UM06-2x energy barriers are around 3 kcal mol^{-1}, so the exchange−correlation functional appears to be far more important than the BSSE corrections, when a basis set as large as aug-cc-pVTZ is used. More specifically, BSSE values for TS1a and TS1b range from 0.2 to 0.3 and 0.1 to 0.3 kcal mol^{-1}, respectively. Similarly, BSSE values for TS2a and TS2b are both equal to 0.1 kcal mol^{-1}. At the CBS-QB3 level of theory, because the basis set is complete, BSSEs are assumed to identically cancel.

Leffler−Hammond's postulate states that the structure of a transition state resembles that of the species nearest to it in free energy.[87] This can be quantified in terms of the position of the transition structure along the reaction coordinate, n_T, as defined by Agmon:[88]

$$n_T = \frac{1}{2 - (\Delta G_r / \Delta G^{\ddagger})} \tag{4}$$

The magnitude of n_T indicates the degree of similarity between the transition structure and the product. According to this equation, the position of the transition state along the reaction coordinate is determined solely by the Gibb's free reaction

Table 3. Internal Energies, Standard Enthalpies, and Gibb's Free Energies (kcal mol⁻¹) of Transition States Relative to the Reactants along the Chemical Pathways 1 and 2 (Figure 3) for the Oxidation of Naphthalene into 1- and 2-Naphthol ($P = 1$ atm) at Different Levels of Theory

species	B3LYP/aug-cc-pVTZ			ωB97XD/aug-cc-pVTZ			UM05-2x/aug-cc-pVTZ			UM06-2x/aug-cc-pVTZ			CBS-QB3			literature $\Delta E^{\ddagger}$ (kcal mol⁻¹)
	$\Delta E_{0K}^{\ddagger}$	$\Delta H^{\circ}_{298K}{}^{\ddagger}$	$\Delta G^{\circ}_{298K}{}^{\ddagger}$	$\Delta E_{0K}^{\ddagger}$	$\Delta H^{\circ}_{298K}{}^{\ddagger}$	$\Delta G^{\circ}_{298K}{}^{\ddagger}$	$\Delta E_{0K}^{\ddagger}$	$\Delta H^{\circ}_{298K}{}^{\ddagger}$	$\Delta G^{\circ}_{298K}{}^{\ddagger}$	$\Delta E_{0K}^{\ddagger}$	$\Delta H^{\circ}_{298K}{}^{\ddagger}$	$\Delta G^{\circ}_{298K}{}^{\ddagger}$	$\Delta E_{0K}^{\ddagger}$	$\Delta H^{\circ}_{298K}{}^{\ddagger}$	$\Delta G^{\circ}_{298K}{}^{\ddagger}$	
naphthalene + OH•	0.0	0.0	0.0	0.0	0.0	0.0	0.0	0.0	0.0	0.0	0.0	0.0	0.0	0.0	0.0	
TS1a	-3.0	-3.6	4.4	-2.3	-3.0	5.1	-1.3	-2.0	6.2	-1.2	-0.9	7.4	-1.5	-2.2	5.9	-3.4[b] -3.6[c] 0.4[d] 0.1[e]
TS1b	-1.8	-2.5	5.8	-0.8	-1.6	6.8	0.1	-0.7	7.7	1.2	0.4	8.8	1.0	0.3	8.6	-2.2[b] -2.6[c] 1.7[d] 1.3[e]
TS1a[a]	-2.8	-3.5	4.6	-2.1	-2.8	5.4	-0.9	-1.7	6.7	-0.9	-0.6	7.6	-1.5	-2.2	5.9	
BSSE energy-TS1a	0.2			0.2			0.3			0.3			0.0			
TS1b[a]	-1.6	-2.3	5.9	-0.6	-1.4	7.0	0.2	-0.6	7.8	1.4	0.7	8.9	1.0	0.3	8.6	
BSSE energy-TS1b	0.2			0.3			0.1			0.3			0.0			
TS2a	10.1	9.2	18.5	8.9	7.9	17.2	7.6	6.6	15.9	5.8	4.8	14.1	6.5	5.5	14.8	
TS2b	10.9	9.9	19.1	10.0	9.0	18.3	9.0	8.1	17.3	7.4	6.4	15.7	9.8	8.9	18.1	
TS2a[a]	10.2	9.2	18.5	9.0	8.0	17.3	7.7	6.7	16.0	7.7	6.7	15.9	6.5	5.5	14.8	
BSSE energy-TS2a	0.1			0.1			0.1			0.1			0.0			
TS2b[a]	10.9	9.9	19.2	10.1	9.1	18.4	9.1	8.2	17.4	7.6	6.6	15.8	9.8	8.9	18.1	
BSSE energy-TS2b	0.1			0.1			0.1			0.1			0.0			

[a] BSSE-corrected relative energies. [b] Reference 27; B3LYP/6-311+G(2df,p) level of theory. [c] Reference 26; B3LYP/6-311G(d) level of theory. [d] Reference 27; BB1K/6-311++G(2df,2p) level of theory. [e] Reference 8; BB1K/6-31+G(d,p) level of theory.

4599

dx.doi.org/10.1021/jp411327e | J. Phys. Chem. A 2014, 118, 4593−4610

Table 4. Internal Energies, Standard Enthalpies, and Gibb's Free Energies (kcal mol⁻¹) of Pre-reactive (IM1) and Post-reactive (IM2) Intermediate States Relative to the Reactants along the Chemical Pathways 1−2 (Figure 3) for the Oxidation of Naphthalene into 1- and 2-Naphthol (P = 1 atm) at Different Levels of Theory

species	B3LYP/aug-cc-pVTZ			ωB97XD/aug-cc-pVTZ			UM05-2x/aug-cc-pVTZ			UM06-2x/aug-cc-pVTZ			CBS-QB3			literature ΔE (kcal mol⁻¹)
	ΔE_{0K}	ΔH°_{298K}	ΔG_{298K}	ΔE_{0K}	ΔH°_{298K}	ΔG_{298K}	ΔE_{0K}	ΔH°_{298K}	ΔG_{298K}	ΔE_{0K}	ΔH°_{298K}	ΔG_{298K}	ΔE_{0K}	ΔH°_{298K}	ΔG_{298K}	
naphthalene + OH•	0.0	0.0	0.0	0.0	0.0	0.0	0.0	0.0	0.0	0.0	0.0	0.0	0.0	0.0	0.0	
IM1 [C₁₀H₈···OH]•	−3.0	−3.1	3.4	−2.9	−3.0	3.2	−3.3	−3.4	2.7	−3.7	−4.2	3.2	−2.5	−2.6	3.7	−1.9[b]
IM1[a]	−2.9	−3.0	3.5	−2.5	−3.1	4.5	−3.1	−3.2	2.9	−3.6	−4.1	3.4	−2.5	−2.6	3.7	
BSSE energy- IM1	0.2	0.2	0.2	0.2	0.0	0.0	0.3	0.2		−0.1	−0.1					
IM2a [C₁₀H₈OH]•	−20.2	−21.1	−12.3	−25.0	−26.0	−17.1	−25.9	−26.8	−18.1	−24.7	−25.7	−16.8	−22.9	−23.8	−15.3	−19.3[b]
IM2b [C₁₀H₈OH]•	−14.1	−14.9	−6.3	−18.1	−18.9	−10.2	−18.5	−19.4	−10.7	−17.6	−18.5	−9.8	−18.4	−19.2	−10.6	−14.4[b]
P1 (1-naphthol + H•)	5.8	6.1	7.9	1.9	2.1	3.9	0.3	0.2	2.7	−0.4	−0.1	1.4	0.6	1.0	2.5	
P2 (2-naphthol + H•)	4.4	4.5	6.6	0.5	0.7	2.8	−0.6	−0.5	1.6	−1.3	−1.2	0.9	−0.3	−0.1	2.0	

[a] BSSE-corrected relative energies. [b] Reference 8; values obtained at the BB1K/6-31+G(d,p) level of theory.
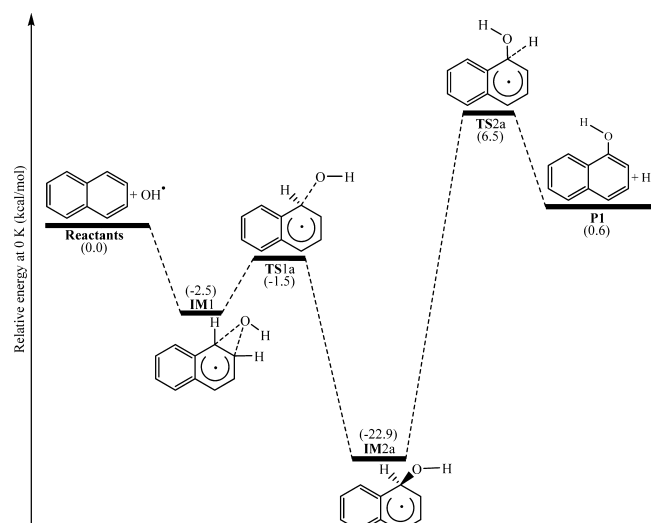

Figure 4. CBS-QB3 energy profile for the reaction pathway **1** characterizing the oxidation of naphthalene by OH radicals into 1-naphthol.
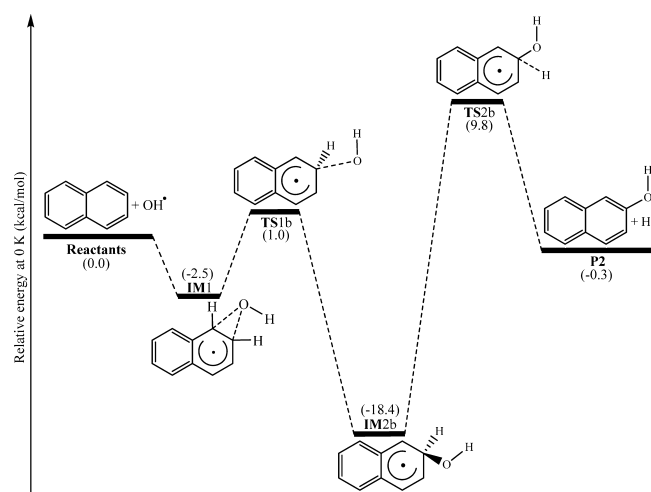

Figure 5. CBS-QB3 energy profile for the reaction pathway **2** characterizing the oxidation of naphthalene by OH radicals into 2-naphthol.

Table 5. Energy Variations (kcal mol⁻¹) along the Chemical Reaction Pathways 1−2 (Figure 3) for the Oxidation of Naphthalene by OH• into 1-Naphthol and 2-Naphthol (Results Obtained at the Benchmark CBS-QB3 Level of Theory, at T = 298.15 K and P = 1.0 atm)

energy diff	step 1		step 2	
	R → IM2a	R → IM2b	IM2a → P1	IM2b → P2
$\Delta E^\ddagger$	−1.5	1.0	29.4	28.2
$\Delta H^{\circ\ddagger}$	−2.2	0.3	29.3	28.0
$\Delta G^{\circ\ddagger}$	5.9	8.6	30.1	28.6
ΔE	−22.9	−18.3	23.6	18.1
ΔH°	−23.8	−19.2	24.7	19.1
ΔG°	−15.3	−10.8	17.8	12.5

energy ΔG_r and the Gibb's free activation energy $\Delta G^\ddagger$. On the basis of our benchmark CBS-QB3 estimates, n_T has values equal to 0.1 and 0.21 for the IM1 → IM2a and IM1 → IM2b reaction steps, respectively. For the IM2a → P1 and IM2b → P2

reaction steps, n_T is found to be equal to 0.71 and 0.64, respectively. In line with the energy profiles and structural observations made in the preceding section, this sequence implies that the TS1a and TS1b transition structures are more similar to the prereactive complex, whereas the TS2a and TS2b transition structures are more similar to the products.

Prior to ending this discussion of reaction energies and energy barriers, it is worth noticing that, at all employed levels of density functional theory, the spin contamination $[\langle S^2 \rangle_{obs} - 0.75]$ never exceeds 0.051 (Table S2 of the Supporting Information) and can thus, for all practical purposes, be regarded as relatively marginal. Some more care is needed for the CBS-QB3 results, because the successive MP2, MP3, MP4SDQ, and CCSD(T) calculations are based on strongly spin-contaminated symmetry-broken unrestricted Hartree–Fock (UHF) wave functions: at this level, the reported $\langle S^2 \rangle$ values are far above 0.75. It is, however, well-known that, in symmetry-breaking situations, the extent of spin contamination decreases with improving treatments of electron correlation,[89] as is precisely the case with CBS-QB3 calculations. Besides, spin contamination for doublet radicals is known to be very small in symmetry-broken UHF-based CCSD calculations, even when the UHF spin contamination is very large.[90] For example, for the NO$_2$ radical, the value of $\langle S^2 \rangle$ is 1.18 and 0.76 for UHF and UHF-based CCSD wave functions, respectively.[90] A CBS-QB3 treatment is therefore expected to progressively compensate the artificial energy lowering[91,92] due to the symmetry breaking of the starting spin-contaminated UHF wave functions (see also refs 93–96), by including correlation corrections of improving quality. We note indeed that, in spite of gigantic spin contamination problems,[94,96] it has been possible to recover on extrapolated CCSD(T)/CBS theoretical grounds the ionization energies, electron attachment energies, and singlet–triplet excitation energies of notoriously difficult compounds like n-acenes ($n = 1-6$) within or very close to chemical accuracy (1 kcal mol^{-1}; i.e., 43 meV, see refs 93, 97, and 98). Whereas the spin contamination observed for the IM1, TS1a, TS1b, and TS2a structures at the UHF level of theory is smaller than the spin contamination observed at the same level for the NO$_2$ radical, the situation seems more problematic with the energized adducts, IM2a and IM2b, and for the transition state (TS2b) associated with the unimolecular dissociation step in the pathway leading to 2-naphthol, which at the HF level yields $\langle S^2 \rangle$ values around 1.55, 1.66, and 1.87 respectively. An essential remark therefore for the forthcoming discussion of kinetic parameters is that, in view of the observed relative spin-contaminations at the HF level (Table S2 of the Supporting Information), the CBS-QB3 energy barrier (TS2b) characterizing the irreversible unimolecular dissociation reaction step in the pathway leading to 2-naphthol may be underestimated by 1–2 kcal mol^{-1}, which may in turn result in an overestimation of the corresponding rate constant (IM2b → P2) by a factor of 10–100. On the other hand, because the IM2b energized adduct is also afflicted by a rather severe spin contamination of the HF electronic wave function (Table S2 of the Supporting Information), this intermediate species is also most likely subject to a comparable energy underestimation, in which case some error compensation is to be expected for the energy difference between the IM2b and TS2b structures.

3.3. Kinetic Parameters. TST and RRKM estimates for individual rate constants are listed in Tables 6 and 7 at a pressure of 1 bar, and at temperatures ranging from 300 to 407 K. In these tables, theoretical rate constants can also be compared with available experimental data.[9,14,18] Further RRKM data computed at lower and higher pressures are provided for the same temperatures in Tables S3a–S3e of the Supporting Information. It is important to note that, on the experimental side,[9,14,18] rate constants were obtained by monitoring continuously the concentration of hydroxyl radical at the entrance of the reaction cell using UV absorption at 194 nm. The experimentally determined rate constants must correspond therefore to the first hydroxyl radical addition step (i.e., the bimolecular reactions R → IM2a + R → IM2b). The reader is referred to Figure 6 for a graphical display of the RRKM estimates for the individual rate constants for these two bimolecular reaction steps at the experimental pressure of 128 mbar[14] and the experimentally available values.[9,14,18] In line with experiment, whatever the pressure (Tables S3a–S3e of the Supporting Information), the TST and RRKM data for the first bimolecular reaction step (R → IM2a) in pathway **1** are all negatively dependent on the temperature, which indicates that, in the first step of the process, OH-addition at the C$_1$ position is favored at the investigated range of temperatures. In contrast, the TST and all RRKM rate constants for the first bimolecular reaction step (R → IM2b) in pathway **2** are positively dependent on the temperature. Tables S3a–S3e of the Supporting Information also confirm that $k_{IM1 \to IM2a}$ and $k_{IM1 \to IM2b}$ are much (at least 10^4 times) smaller than $k_{IM1 \to R}$, an observation that validates the steady state analysis leading to eq 1.

The fact that the first bimolecular reaction step on pathway **1** is characterized by a slightly negative energy barrier whereas on pathway **2** it is characterized by a small positive energy barrier is conceptually not entirely sufficient, however, to explain why the production of 1-naphthol (P1) was experimentally found[26] to be favored by a factor 2:1 with respect to the production of 2-naphtol (P2). To check this fully on safe enough theoretical ground, one must evaluate effective kinetic rate constants that also account for the second unimolecular dissociation reaction step.

Indeed, the supplied TST and RRKM results (Tables 6 and 7) indicate that, at $P = 1$ bar, the postreactive intermediate IM2b decomposes ~10 times faster than the postreactive intermediate IM2a, which seems also consistent with the view that the formation of 2-naphthol (P2) dominates the formation of 1-naphthol (P1) under ambient pressure, in the absence of molecular oxygen. According to the RRKM results (Tables S4a–S4j of the Supporting Information), this is only at pressures smaller than 0.1 mbar that deviations from the high pressure limit start to become numerically detectable (i.e., larger than ~1%) for these reaction steps (IM2a → P1, or IM2b → P2). Nevertheless, at such exceedingly low pressures, further careful analyses employing the Master-Equation approach[99] are needed for quantitatively evaluating the outcome of additions of hydroxyl radicals on naphthalene away from chemical equilibrium, and under an inert (He) atmosphere.

To evaluate effective rate constants for the two competitive pathways (**1**, **2**) that prevail in the absence of molecular oxygen, and in view of the original hypothesis by Lorenz and Zellner,[14] we assume that the kinetics of the whole reaction can be modeled according to a two-step mechanism, involving first a fast and reversible pre-equilibrium between the reactants (C$_{10}$H$_8$ and OH radicals) and energized adducts (IM2x with x = a, b), followed by an irreversible dissociation step (breaking of C–H bond) leading to 1- and 2-naphthol (the products, P1 and P2):

Table 6. Rate Constants (Units: Unimolecular Reactions in s^{-1}; Bimolecular Reactions in cm^3 molecule^{-1} s^{-1}), Effective Rate Constants, and Branching Ratios for the Reported Reaction Channels by Means of TST Theory ($P = 1$ bar), According to the Computed CBS-QB3 Energy Profiles (See Computational Details Section)

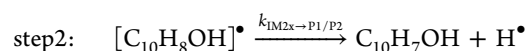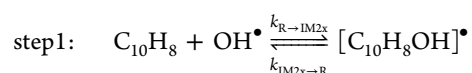| T (K)	rate constant						effective rate constant		branching ratio		k_{exp} [9,14,18]
	R → IM2a	R → IM2b	IM2a → R	IM2b → R	IM2a → P1	IM2b → P2	R → P1	R → P2	R(1)	R(2)	
300	4.49×10^{-14}	7.91×10^{-15}	3.12×10^{-2}	4.98×10^{-1}	2.76×10^{-6}	2.90×10^{-5}	3.97×10^{-18}	4.61×10^{-19}	89.61	10.39	$(18.6 \pm 1.0) \times 10^{-12}$
337	3.74×10^{-14}	1.41×10^{-14}	1.57×10^{0}	1.47×10^{1}	2.65×10^{-4}	2.18×10^{-3}	6.31×10^{-18}	2.09×10^{-18}	75.12	24.88	$(14.6 \pm 5.0) \times 10^{-12}$
358	3.46×10^{-14}	1.87×10^{-14}	8.90×10^{0}	7.55×10^{1}	2.37×10^{-3}	1.72×10^{-2}	9.21×10^{-18}	4.26×10^{-18}	68.38	31.62	$(11.0 \pm 4.4) \times 10^{-12}$
378	3.26×10^{-14}	2.40×10^{-14}	3.78×10^{1}	3.11×10^{2}	1.51×10^{-2}	9.84×10^{-2}	1.30×10^{-17}	7.59×10^{-18}	63.17	36.83	$(10.1 \pm 4.0) \times 10^{-12}$
407	3.06×10^{-14}	3.33×10^{-14}	2.38×10^{2}	1.96×10^{3}	1.56×10^{-1}	9.08×10^{-1}	2.00×10^{-17}	1.54×10^{-17}	56.52	43.48	$(10.5 \pm 4.0) \times 10^{-12}$

Table 7. Rate Constants (Units: Unimolecular Reactions in s^{-1}; Bimolecular Reactions in cm^3 molecule^{-1} s^{-1}), Effective Rate Constants, and Branching Ratios for the Reported Reaction Channels by Means of RRKM Theory ($P = 1$ bar), According to the Computed CBS-QB3 Energy Profiles (See Computational Details Section)

T (K)	rate constant						effective rate constant		branching ratio		k_{exp} [9,14,18]
	R → IM2a	R → IM2b	IM2a → R	IM2b → R	IM2a → P1	IM2b → P2	R → P1	R → P2	R(1)	R(2)	
300	2.92×10^{-14}	4.65×10^{-15}	2.87×10^{-2}	4.91×10^{-1}	1.47×10^{-6}	1.37×10^{-5}	1.50×10^{-18}	1.30×10^{-19}	92.02	7.98	$(18.6 \pm 1.0) \times 10^{-12}$
337	2.48×10^{-14}	6.76×10^{-15}	1.28×10^{0}	1.57×10^{1}	1.59×10^{-4}	1.19×10^{-3}	3.08×10^{-18}	5.12×10^{-19}	85.74	14.26	$(14.6 \pm 5.0) \times 10^{-12}$
358	2.31×10^{-14}	7.93×10^{-15}	7.86×10^{0}	8.22×10^{1}	1.48×10^{-3}	1.00×10^{-2}	4.35×10^{-18}	9.65×10^{-19}	81.85	18.15	$(11.0 \pm 4.4) \times 10^{-12}$
378	2.19×10^{-14}	9.02×10^{-15}	3.67×10^{1}	3.35×10^{2}	9.92×10^{-3}	6.13×10^{-2}	5.89×10^{-18}	1.65×10^{-18}	78.12	21.88	$(10.1 \pm 4.0) \times 10^{-12}$
407	2.03×10^{-14}	1.04×10^{-14}	2.63×10^{2}	2.02×10^{3}	1.13×10^{-1}	6.23×10^{-1}	8.76×10^{-18}	3.21×10^{-18}	73.21	26.79	$(10.5 \pm 4.0) \times 10^{-12}$
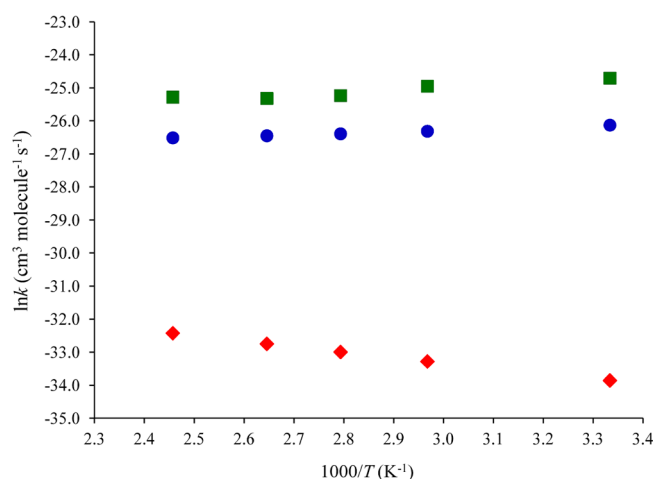
Figure 6. Arrhenius plot of the obtained RRKM bimolecular rate constants (for R → IM2x, with x = a, b) versus experiment. Legend: (●) theoretical rate constant for pathway **1**; (◆) theoretical rate constant for pathway **2**; (■) experimental data.[9,14,18]

step1: $C_{10}H_8 + OH^{\bullet} \underset{k_{IM2x\to R}}{\overset{k_{R\to IM2x}}{\rightleftharpoons}} [C_{10}H_8OH]^{\bullet}$

step2: $[C_{10}H_8OH]^{\bullet} \xrightarrow{k_{IM2x\to P1/P2}} C_{10}H_7OH + H^{\bullet}$

The second step is assumed to be irreversible, because the original experience by Lorenz and Zellner[14] was performed under steady flow conditions in the reaction cell, implying continuous displacements of the reaction toward the formation of 1- and 2-naphthol. Therefore, a steady state analysis upon the above sequence of reactions leads to the following expressions for the effective rate constants characterizing pathways **1** and **2**:

$$k_{eff}(1) = \frac{k_{R\to IM2a}k_{IM2a\to P1}}{k_{IM2a\to R} + k_{IM2a\to P1}} \quad (5)$$

$$k_{eff}(2) = \frac{k_{R\to IM2b}k_{IM2b\to P2}}{k_{IM2b\to R} + k_{IM2b\to P2}} \quad (6)$$

In the above equations, $k_{R\to IM2x}$ is the kinetic rate constant characterizing the forward bimolecular reaction step (in cm^3 $molecule^{-1}$ s^{-1}), whereas $k_{IM2x\to P}$ and $k_{IM2x\to R}$ represent the forward and backward unimolecular reaction rate constants (in s^{-1}). The supplied RRKM data (Tables S4a−S4j of the Supporting Information) indicate that, from 1 bar down to pressures of 0.01 mbar, $k_{IM2a\to P1}$ and $k_{IM2b\to P2}$ are much (at least 10^3 times) smaller than $k_{IM2a\to R}$ and $k_{IM2b\to R}$, respectively, and can thus be neglected from the above denominators. This implies further that, at pressures larger than 0.01 mbar:

$$k_{eff}(1) = K_c(1)k_{IM2a\to P1} \quad (7)$$

$$k_{eff}(2) = K_c(2)k_{IM2b\to P2} \quad (8)$$

where $K_c(1)$ and $K_c(2)$ are the relevant equilibrium constants for the pre-equilibrium between the reactants and the energized adducts:

$$K_c(1) = \frac{k_{R\to IM2a}}{k_{IM2a\to R}} = \frac{[IM2a]}{[C_{10}H_8][OH^{\bullet}]} \quad (9)$$

$$K_c(2) = \frac{k_{R\to IM2b}}{k_{IM2b\to R}} = \frac{[IM2b]}{[C_{10}H_8][OH^{\bullet}]} \quad (10)$$

Equations 7−10 show that the overall kinetics of the hydroxyl radical addition pathways on naphthalene does not depend upon the energy barriers characterizing the first bimolecular rate constants, but upon the Gibb's free energy differences between the reactants and the energized adducts $[C_{10}H_8OH^{\bullet}]$ (IM1a, IM1b) as well as upon the energy barriers characterizing the subsequent unimolecular dissociation reaction steps (i.e., cleavages of C−H bonds). We correspondingly report in Tables 6 and 7, as well as in Tables S4a−S4j of the Supporting Information, branching ratios, which were obtained according to

$$R(1) = \frac{k_{eff}(1)}{k_{eff}(1) + k_{eff}(2)} \quad (11)$$

and

$$R(2) = \frac{k_{eff}(2)}{k_{eff}(1) + k_{eff}(2)} \quad (12)$$

using eqs 5 and 6 for computing $k_{eff}(1)$ and $k_{eff}(2)$. These data indicate that, at all considered pressures, and qualitatively in line with the theoretical analysis by Ricca and Bauschlischer,[26] as well as with the experimental observation they invoke from a personal communication by M. P. Bernstein, the most abundant product resulting from the oxidation of naphthalene by OH radicals is undoubtedly 1-naphthol (P1). This conclusion will most certainly remain valid at better theoretical levels than CBS-QB3, because we expect this approach to slightly underestimate, by 1−2 kcal mol^{-1}, the energy barrier (TS2b) characterizing the irreversible dissociation step in the pathway leading to 2-naphthol, and to yield in turn an overestimation by a factor 10−100 of the corresponding rate constant (IM2b → P2), relative to the constant characterizing the other dissociation pathway (IM2a → P1). In view of the supplied RRKM data (Tables S4a−S4j of the Supporting Information), it is thus more than certain that, at 300 K, the production of 1-naphthol must dominate the overall reaction mechanism, and this down to extremely low pressures, larger than 10^{-8} bar. From these data, and the correspondingly computed regioselectivity indices [RSI = $R(1) − R(2)$, Figure 7], we also note overall a decrease of the regioselectivity of the reaction with increasing temperatures and lowering pressures.

The production of 1-naphthol over 2-naphthol with a ratio 2:1 is observed for instance at P = 0.001 bar and at T around 337 K. Lacking any information on the conditions under which the experiments by M. P. Bernstein were made, we can only strongly advocate further detailed experimental studies of the oxidation mechanisms of naphthalene by OH radicals, to verify the relevance of our theoretical estimates for branching ratios.

Experimental kinetic rate constants ascribed to the first bimolecular reaction steps (R → IM2a and R → IM2b) in pathways **1** and **2** can be compared with the corresponding RRKM data displayed in Figure 6, for a pressure of 128 mbar. Our theoretical rate constants for these reaction steps were fitted by means of least-squares regressions to a three-parameter Arrhenius equation ($k = AT^n e^{-B/RT}$), to obtain the exponent n, the effective preexponential factor A, and the activation barrier B which characterize pathways **1** and **2** according to the decay rate of the concentration of hydroxyl radicals. This fitting procedure led correspondingly to the following expressions: $k_1(T) = 1.02 \times 10^{-14}T^{-0.369} \exp(340.4/T)$, and $k_2(T) = 2.72 \times 10^{-10}T^{-1.544} \exp(-990.9/T)$ cm^3 $molecule^{-1}$ s^{-1}, respectively, at
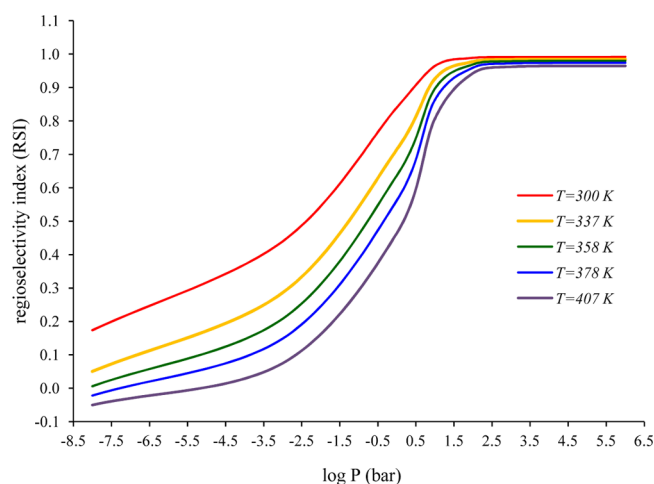
Figure 7. Dependence upon the pressure and temperature of the regioselectivity $[\text{RSI} = R(1) - R(2)]$ of OH radical addition on naphthalene, according to the RRKM estimates of effective rate constants $[k_{\text{eff}}(1), k_{\text{eff}}(2)]$ supplied in Tables S4a−S4j (Supporting Information).

a pressure of 128 mbar and over the temperature range 300−407 K. We emphasize again that, at pressures lower than 10 bar, and in line with the experimental observations by Lorenz and Zellner,[14] the rate constants characterizing the first bimolecular reaction steps R → IM2a and R → IM2b decrease and increase, respectively, as the temperature increases (Tables S4a−S4j of the Supporting Information).

More specifically, from Figure 8 and Table 8, it is clear that, at the experimental pressure of 128 mbar,[14] the RRKM rate constants obtained from the CBS-QB3 energy profiles for the R → IM2a reaction step along the chemical pathway leading to 1-naphthol underestimate the experimental ones by about 2 orders of magnitude only. Both the experimental rate constants and theoretical rate constants for this reaction step decrease with increasing temperatures. This qualitatively excellent agreement between theory and experiment makes us believe that the physical chemistry of these complicated processes has been correctly captured: it confirms the relevance of both the proposed reaction mechanism and employed quantum chemical models. Note that the overall rate constants reported in Table 8 for the formation of 1-naphthol or 2-naphthol indicate that this reaction is too slow to compete with further reaction channels. Most likely, in the experiment by Lorenz and Zellner,[14] removal of the intermediate adducts IM2a and IM2b is most likely to be ascribed to recombination with further OH radicals.

When Tables 6 and 7 and Table S4e of the Supporting Information are compared, it appears that TST and RRKM data at 1 bar are not all strictly equal, indicating that the high pressure limit has not been reached at this pressure for all considered reaction channels. Very interestingly, upon scrutinizing further the RRKM values in Tables S4a−S4j of the Supporting Information, the high (infinite) pressure limit for the IM2x → Px, IM2x → R, and IM1 → IM2b reaction steps is reached within 1% accuracy when the pressure exceeds 10^{-4}, 10^{-3}, and 10^2 bar, respectively, whatever the temperature (see also Figure 9 for a logarithmic plot of the bimolecular rate constants for the R → IM2a and R → IM2b reaction steps as a function of the pressure and temperature). These observations can be correlated with energy barriers equal to 28.2 or 29.4, 21.4 or 19.4, and 3.5 kcal mol^{-1}, respectively. In line with an effective negative energy barrier (-1 kcal mol^{-1}), this is only at a
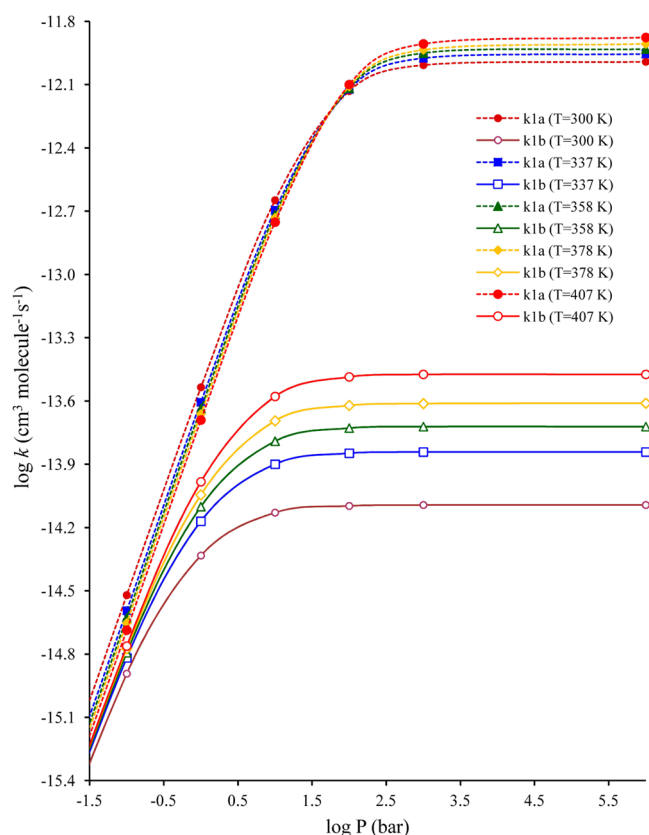
Figure 8. Pressure dependence of the bimolecular rate constants for the R → IM2a (k1a) and R → IM2b (k1b) reaction steps (RRKM results, obtained by means of eq 3).

pressure of 10^3 bar that some convergence to the high pressure limit starts to be seen for the IM1 → IM2a reaction step. More specifically, Figures 8 and 9 and the kinetic data supplied in the Supporting Information show that pressures larger than 10^5 bar are required for restoring the validity of the transition state approximation for the first bimolecular reaction steps within ∼5% accuracy. Besides the low or even negative energy barriers, such a high pressure value may also be the consequence of the large molecular volume of the reactant and the extent of the depth (∼100 kJ/mol) of the interaction well between naphthalene and hydroxyl radicals.

3.4. Bond Order Analysis. A balanced measure of the extent of bond formation or bond breaking along a reaction pathway is provided by the concept of bond order (B), a concept that has often been used to investigate the molecular mechanism of chemical reactions.[100] To follow the nature of the process, Wiberg bond indices have been computed according to a NBO analysis,[45,101] as implemented in Gaussian 09. There are several breaking/forming bond processes along the fragmentation process and the global nature of the reaction can be monitored by means of the so-called synchronicity (S_y),[102] defined by the following expression:

$$S_y = 1 - \frac{\left[\sum_{i=1}^{n} \frac{|\delta B_i - \delta B_{\text{av}}|}{\delta B_{\text{av}}}\right]}{2n - 2} \tag{13}$$

In the above equation, n is the number of bonds directly involved in the reaction and the relative variation of the bond index (δB_i) for a bond i at the transition state (TS) is estimated according to

Table 8. Rate Constants (Units: Unimolecular Reactions in s⁻¹; Bimolecular Reactions in cm³ molecule⁻¹ s⁻¹), Effective Rate Constants, and Branching Ratios for the Reported Reaction Channels by Means of RRKM Theory (P = 128 mbar)

T (K)	rate constant						effective rate constant		branching ratio		k_{exp}[9,14,18]
	R → IM2a	R → IM2b	IM2a → R	IM2b → R	IM2a → P1	IM2b → P2	R → P1	R → P2	R(1)	R(2)	
300	3.87×10^{-15}	1.49×10^{-15}	2.87×10^{-2}	4.90×10^{-1}	1.47×10^{-6}	1.37×10^{-5}	1.98×10^{-19}	4.17×10^{-20}	82.63	17.37	$(18.6 \pm 1.0) \times 10^{-12}$
337	3.26×10^{-15}	1.81×10^{-15}	1.28×10^{0}	1.57×10^{1}	1.59×10^{-4}	1.19×10^{-3}	4.05×10^{-19}	1.37×10^{-19}	74.69	25.31	$(14.6 \pm 5.0) \times 10^{-12}$
358	3.02×10^{-15}	1.93×10^{-15}	7.84×10^{0}	8.16×10^{1}	1.48×10^{-3}	1.00×10^{-2}	5.70×10^{-19}	2.36×10^{-19}	70.68	29.32	$(11.0 \pm 4.4) \times 10^{-12}$
378	2.85×10^{-15}	2.03×10^{-15}	3.65×10^{1}	3.32×10^{2}	9.91×10^{-3}	6.13×10^{-2}	7.74×10^{-19}	3.75×10^{-19}	67.37	32.63	$(10.1 \pm 4.0) \times 10^{-12}$
407	2.64×10^{-15}	2.10×10^{-15}	2.61×10^{2}	1.98×10^{3}	1.13×10^{-1}	6.23×10^{-1}	1.14×10^{-18}	6.61×10^{-19}	63.36	36.64	$(10.5 \pm 4.0) \times 10^{-12}$

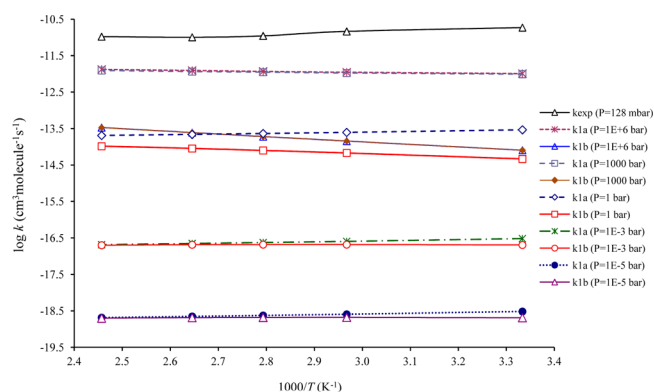**Figure 9.** Arrhenius plot of the RRKM bimolecular rate constants (k1x, with x = a,b) for the R → IM2x (x = a,b) reaction steps.

$$\delta B_i = \frac{B_i^{TS} - B_i^{R}}{B_i^{IM2x} - B_i^{R}} \tag{14}$$

where the superscripts R and IM2x refer to the reactant and postreactive complexes (IM2a or IM2b), respectively. The relative change in bond order is ultimately given as a percentage:

$$\%EV = \delta B_i \times 100 \tag{15}$$

The average change in bond order is obtained from

$$\delta B_{av} = \frac{1}{n} \sum_{i=1}^{n} \delta B_i \tag{16}$$

Bond indices were calculated for the $n = 9$ bonds, which were substantially altered by hydroxyl radical addition; namely, the C_1-C_2, C_2-C_3, C_3-C_4, C_4-C_{10}, C_9-C_{10}, C_1-C_9, C_1-O, C_2-O, and $O-H$ bonds (Figure 2); all other bonds remain practically unaltered during the reaction. The calculated Wiberg bond indices B_i for the reactants ($C_{10}H_8$ and OH), transition states (TS1a and TS1b), and postreactive complexes (IM2a and IM2b) enable us (Table 9) to examine the progress of the reactions **1** and **2** and position of the transition states between reactants and products. For both reactions, according to the relative changes in bond order, the most strongly affected chemical bond is C_1-C_2, which during the process becomes a single C−C bond. The chemical reaction pathways **1** and **2** are characterized by a synchronicity value around ∼0.87, which reveals a chemical process that is concerted, but not fully synchronic.

3.5. Natural Bond Orbital (NBO) Analysis. Delocalization of electron density among the filled (bonding or lone pair) Lewis type NBOs and the empty (antibonding and Rydberg) non-Lewis NBOs leads to transfer of occupancy from the localized NBOs of the idealized Lewis structure into the empty non-Lewis orbitals and, thus, a departure from an idealized Lewis structure description. This transfer is referred to as a "delocalization" correction to the zero-order natural Lewis structure through a stabilizing donor−acceptor interaction. The energies of these interactions can be estimated by second-order perturbation theory.[46] For each donor NBO(i) and acceptor NBO(j), the stabilization energy (E_2) associated with the $i \rightarrow j$ delocalization can be estimated according to the following equation:[103]

$$E_2 = \Delta E_{ij} = q_i \left[\frac{F_{(i,j)}^2}{\varepsilon_i - \varepsilon_j} \right] \tag{17}$$

Table 9. Bond Order Analysis of Structures Involved in the Chemical Reaction Pathways 1 and 2 at the B3LYP/6-311G(2d,d,p) Level of Theory[a]

pathway		C_1-C_2	C_2-C_3	C_3-C_4	C_4-C_{10}	C_9-C_{10}	C_1-C_9	C_1-O	C_2-O	$O-H$	δB_{av}	S_y
1	$B_i(R)$	1.554	1.310	1.554	1.272	1.232	1.272	0.000		0.857	0.230	0.868
	$B_i(TS1a)$	1.395	1.344	1.519	1.250	1.242	1.209	0.224		0.837		
	$B_i(IM2a)$	1.030	1.572	1.338	1.195	1.287	0.999	0.891		0.789		
	%EV	30.461	13.138	16.244	28.405	18.464	23.147	25.146		29.308		
2	$B_i(R)$	1.554	1.310	1.554	1.272	1.232	1.272		0.000	0.857	0.296	0.874
	$B_i(TS1b)$	1.364	1.216	1.618	1.220	1.221	1.287		0.283	0.833		
	$B_i(IM2b)$	1.038	1.022	1.799	1.126	1.179	1.376		0.881	0.791		
	%EV	36.791	32.453	26.187	35.817	21.869	14.491		32.092	36.732		

[a]Wiberg bond indexes (B_i), % evolution through the reaction coordinate (%EV), average bond index variation (δB_{av}), and Synchronicity parameter (S_y) are shown.

where q_i is the donor orbital occupancy, ε_i and ε_j are diagonal elements (orbital energies) of the NBO Fock matrix, and $F_{(i,j)}$ are off-diagonal elements of this matrix.

Based on the B3LYP/6-311G(2d,d,p) optimized geometries and electronic structure characteristics of the IM2a and IM2b energized adducts, the NBO analysis of donor−acceptor interactions (Table 10) shows that the stabilization energies associated

Table 10. NBO Occupancies and Stabilization Energies (kcal mol^{-1}) Characterizing Intermediate and Transition Structures along the Chemical Reaction Pathways 1 and 2 (Results Obtained at the B3LYP/6-311G(2d,d,p) Level of Theory)

	B3LYP/6-311G(2d,d,p)			
	IM2a	IM2b	TS1a	TS1b
		Occupancies		
$\sigma(C_1-C_2)$	0.9902	0.9906	0.9902	0.9904
$\sigma^*(C_1-C_2)$	0.0149	0.0140	0.0071	0.0071
$\pi(C_1-C_2)$		0.8116	0.8499	0.8584
$\pi^*(C_1-C_2)$		0.4909	0.1426	0.1532
$n_{O(1)}$	0.9923	0.9925	0.9983	0.9983
$n_{O(2)}$	0.9792	0.9800	0.9922	0.9898
$n_{O(3)}$			0.9587	0.9411
		Stabilization Energies (E_2)		
$n_{O(1)} \rightarrow \sigma^*(C_1-C_2)$	3.28	3.27		0.03
$n_{O(1)} \rightarrow \pi^*(C_1-C_2)$		5.08	0.97	1.48
$n_{O(2)} \rightarrow \pi^*(C_1-C_2)$		1.03		0.16
$n_{O(3)} \rightarrow \pi^*(C_1-C_2)$			8.88	14.17

with the electron delocalization from nonbonding oxygen lone-pair orbitals $[n_O]$ to $\sigma^*(C_1-C_2)$ antibonding orbitals are around 3.3 kcal mol^{-1}. According to the NBO analysis, the $\sigma(C_1-C_2)$ bonding orbital occupancies in these systems are both equal to 0.99, whereas the $\sigma^*(C_1-C_2)$ antibonding orbital occupancies in the energized adducts IM2a and IM2b amount to 0.015 and 0.014, respectively.

In the TS1a and TS1b transition states, there are two nonbonding oxygen lone pairs and one unpaired electron on the oxygen atom, whereas in the IM2a and IM2b intermediates, there are only two nonbonding oxygen lone pairs $[n_O]$. Inspection of the NBO data reported in Table 10 for the TS1a and TS1b transition states reveals that a very strong interaction prevails in between one of the oxygen lone pairs of the hydroxyl radical and the unoccupied $\pi^*(C_1-C_2)$ orbital, resulting for the latter orbital in an occupancy around 0.15. The corresponding stabilization energies range from 8.9 to 14.2 kcal mol^{-1}. These results are in line with the donation of one electron from OH$^\bullet$

to the $\pi^*(C_1-C_2)$ orbital, during the oxidation process. The NBO analysis demonstrates therefore that anomeric $[n_O \rightarrow \sigma^*_{C1-C2}]$ and hyperconjugative $[n_O \rightarrow \pi^*_{C1-C2}]$ interactions have a significant influence on the computed activation energies and reaction energies. Nevertheless, it appears that the delocalization energy for TS1a is 5.3 kcal mol^{-1} smaller than that for TS1b (Table 10), whereas the [B3LYP/6-311G(2d,d,p)] energy of TS1a is 2.5 kcal mol^{-1} lower than that of TS1b (Table 3). These observations indicate that aromatic effects dominate anomeric and hyperconjugation effects, as one would quite naturally expect.

4. CONCLUSIONS

The oxidation mechanisms of naphthalene initiated by OH radicals in the gas phase have been studied computationally using density functional theory along with various exchange−correlation functionals (B3LYP, ωB97XD, UM05-2x, and UM06-2x) and an extremely large basis set (aug-cc-pVTZ). The supplied reaction energies and activation barriers incorporate zero-point vibrational energy differences and counterpoise corrections for basis set superposition errors. Comparison has been made with benchmark computational results obtained at the composite CBS-QB3 level of theory. The best agreement with the computed reaction energies and energy barriers is obtained with the UM05-2x exchange−correlation functional. Kinetic rate constants were correspondingly estimated in the high pressure limit by means of transition state theory, on the grounds of partition functions calculated using the rigid rotor-harmonic oscillator (RRHO) approximation. Their pressure dependence has been investigated by means of statistical Rice−Ramsperger−Kassel−Marcus (RRKM) theory. The main focus of the present paper was on the reaction steps involved in the so-called hydroxyl radical addition pathway. Note that the reaction mechanisms involved in the so-called hydrogen abstraction pathway will be subject of a separate study,[104] on similar theoretical CBS-QB3 and DFT grounds.

The obtained results indicate that the experimental rate constants supplied by Atkinson[9] correspond to a bimolecular reaction step leading to a molecular energized adduct $[C_{10}H_8OH^\bullet]$. This first reaction step is strongly exergonic at ambient temperature and pressure. In line with experiment, due to the formation of a prereactive van der Waals (VdW) molecular complex $[C_{10}H_8 \cdots OH]^\bullet$, the corresponding transition state lies below the reactant, hence an effective negative activation energy around −1.5 kcal mol^{-1} on the reaction pathway leading to 1-naphthol. In contrast, on the reaction pathway leading to 2-naphthol, the first bimolecular reaction step is characterized by a positive activation energy, around 1 kcal mol^{-1}.

The formation of the energized adduct is followed by a unimolecular reaction step that is strongly endergonic at ambient temperature and pressure, and which corresponds to the elimination of a H atom (H•), yielding 1- or 2-naphthol. Effective rate constants have been calculated according to a steady state analysis upon to a two-step model reaction mechanism, assuming reversibility of the first bimolecular addition reaction step, and irreversibility of the second unimolecular dissociation step. In line with the experimental observations by Lorenz and Zellner,[14] the correspondingly obtained branching ratios indicate that the most abundant product resulting from the oxidation of naphthalene by OH radicals must be 1-naphthol rather than 2-naphthol. These branching ratios also indicate that the regioselectivity of the OH•-addition pathways onto naphthalene decrease with increasing temperatures and decreasing pressures. In line with slightly positive or even negative activation energies, it was found that the transition state approximation breaks down at ambient pressure (1 bar) for the first bimolecular reaction steps. This is particularly true for the first bimolecular reaction step involved in the OH•-addition pathway leading to 1-naphthol, which is characterized by an effective activation energy of -1.5 kcal mol^{-1}. RRKM calculations show in particular that overwhelmingly high pressures, larger than 10^5 bar, would be required for restoring within ~5% accuracy the validity of this approximation for *all* reaction channels in the OH-addition pathway, in particular for the conversion of the prereactive van der Waals (VdW) complex $[C_{10}H_8\cdots OH]^\bullet$ into the molecular energized adduct $C_{10}H_8OH^\bullet$.

Analysis of the computed structures, bond orders, and free energy profiles demonstrate that the reaction steps involved in the oxidation of naphthalene by OH radicals satisfy Leffler−Hammond's principle: the transition states for the exergonic bimolecular reaction steps are structurally closer to the prereactive VdW complexes, whereas the transition states for the subsequent endergonic unimolecular reaction steps are structurally closer to the products, 1- or 2-naphthol. NICS indices and natural bond orbital analysis also show that the computed activation and reaction energies are largely dictated by alterations of aromaticity and, to a lesser extent, by anomeric and hyperconjugative effects pertaining to the delocalization of oxygen lone pairs to neighboring empty σ^*_{C1-C2} and π^*_{C1-C2} orbitals.

■ ASSOCIATED CONTENT

ⓢ Supporting Information

Supplementary data (Tables S1−S4) associated with this article can be found, in the online version. Table S1: Eckart tunneling factor for the final unimolecular dissociation reaction step at temperatures ranging from 300 to 407 K. Table S2: Expectation value of the S^2 operator at the reported theoretical levels. Table S3: Kinetic rate constants for the first bimolecular reaction step involved in the chemical pathways **1−2** at different pressure and temperatures using RRKM theory. Table S4: Kinetic rate constants for all reaction steps involved in the chemical pathways **1−2** at different pressures and temperatures using the RRKM theory. This material is available free of charge via the Internet at http://pubs.acs.org.

■ AUTHOR INFORMATION

Corresponding Author

*M. S. Deleuze: tel, +32-11-268303; e-mail, michael.deleuze@uhasselt.be.

■ REFERENCES

(1) Tokiwa, H.; Ohnishi, Y.; Rosenkranz, H. S. Mutagenicity and Carcinogenicity of Nitroarenes and Their Sources in the Environment. *CRC Crit. Rev. Toxicol.* **1986**, *17*, 23−60.

(2) Josephy, P. D.; Mannervik, B.; De Montellano, P. O. *Molecular Toxicology*; Oxford University Press: Oxford, U.K., 1997.

(3) Mastral, A. M.; Callen, M. S. A Review on Polycyclic Aromatic Hydrocarbon (PAH) Emissions from Energy Generation. *Environ. Sci. Technol.* **2000**, *34*, 3051−3057.

(4) Boström, C. E.; Gerde, P.; Hanberg, A.; Jernström, B.; Johansson, C.; Kyrklund, T.; Rannug, A.; Törnqvist, M.; Victorin, K.; Westerholm, R. Cancer Risk Assessment, Indicators, and Guidelines for Polycyclic Aromatic Hydrocarbons in the Ambient Air. *Environ. Health Perspect.* **2002**, *110*, 451−488.

(5) Baek, S. O.; Field, R. A.; Goldstone, M. E.; Kirk, P. W.; Lester, J. N.; Perry, R. A Review of Atmospheric Polycyclic Aromatic Hydrocarbons: Sources, Fate and Behavior. *Water, Air, Soil Pollut.* **1991**, *60*, 279−300.

(6) Bunce, N. J.; Liu, L.; Zhu, J. Reaction of Naphthalene and Its Derivatives with Hydroxyl Radicals in the Gas Phase. *Environ. Sci. Technol.* **1997**, *31*, 2252−2259.

(7) Atkinson, R.; Arey, J. Atmospheric Chemistry of Gas-Phase Polycyclic Aromatic Hydrocarbons: Formation of Atmospheric Mutagens. *Environ. Health Perspect.* **1994**, *102*, 117−126.

(8) Qu, X.; Zhang, Q.; Wang, W. Mechanism for OH-Initiated Photooxidation of Naphthalene in the Presence of O$_2$ and NO$_x$: A DFT Study. *Chem. Phys. Lett.* **2006**, *429*, 77−85.

(9) Atkinson, R. Kinetics and Mechanisms of the Gas-Phase Reactions of the Hydroxyl with Organic Compounds. *J. Phys. Chem. Ref. Data, Monograph* **1989**, *1*, 1−246.

(10) Atkinson, R.; Tuazon, E. C.; Arey, J. Reactions of Naphthalene in N$_2$O$_5$-NO$_3$-NO$_2$-Air Mixtures. *Int. J. Chem. Kinet.* **1990**, *22*, 1071−1082.

(11) Atkinson, R. Kinetics and Mechanisms of the Gas-Phase Reactions of the NO$_3$ Radical with Organic Compounds. *J. Phys. Chem. Ref. Data, Monograph* **1991**, *20*, 459−507.

(12) Atkinson, R.; Tuazon, E. C.; Bridier, I.; Arey, J. Reactions of NO$_3$-Naphthalene Adducts with O$_2$ and NO$_2$. *Int. J. Chem. Kinet.* **1994**, *26*, 605−614.

(13) Sasaki, J.; Aschmann, S. M.; Kwok, E. S. C.; Atkinson, R.; Arey, J. Products of the Gas-Phase OH and NO$_3$ Radical-Initiated Reactions of Naphthalene. *Environ. Sci. Technol.* **1997**, *31*, 3173−3179.

(14) Lorenz, K.; Zellner, R. Kinetics of the Reactions of OH-Radicals with Benzene, Benzene-d$_6$ and Naphthalene. *Ber. Bunsen-Ges. Phys. Chem.* **1983**, *87*, 629−636.

(15) Arey, J.; Zielinska, B.; Atkinson, R.; Winer, A. M. Polycyclic Aromatic Hydrocarbon and Nitroarene Concentrations in Ambient Air During a Wintertime High-NO$_x$ Episode in the Los Angeles Basin. *Atmos. Environ.* **1967**, *21*, 1437−1444.

(16) Arey, J.; Atkinson, R.; Zielinska, B.; McElroy, P. A. Diurnal Concentrations of Volatile Polycyclic Aromatic Hydrocarbons and

Nitroarenes during a Photochemical Air Pollution Episode in Glendora. California. *Environ. Sci. Technol.* **1989**, *23*, 321−327.

(17) Durant, J. L.; Lafleur, A. L.; Plummer, E. F.; Taghizadeh, K.; Busby, W. F.; Thilly, W. G. Human Lymphoblast Mutagens in Urban Airborne Particles. *Environ. Sci. Technol.* **1998**, *32*, 1894−1906.

(18) Lorenz, K.; Zellner, R. Kinetics of the Reactions of OH Radicals with Benzene, Naphthalene, and Phenanthrene between 400 and 1000 K. *8th International Symposium on Gas Kinetics*; University of Nottingham, Nottingham, U.K., 15-20 July, 1984.

(19) Atkinson, R.; Aschmann, S. M.; Pitts, J. N. Kinetics of the Reactions of Naphthalene and Biphenyl with Hydroxyl Radicals and with Ozone at 294 ± 1 K. *Environ. Sci. Technol.* **1984**, *18*, 110−113.

(20) Biermann, H. W.; Mac Leod, H.; Atkinson, R.; Winer, A. M.; Pitts, J. N. Kinetics of the Gas-Phase Reactions of the Hydroxyl Radical with Naphthalene, Phenanthrene, and Anthracene. *Environ. Sci. Technol.* **1985**, *19*, 244−248.

(21) Atkinson, R.; Aschmann, S. M. Kinetics of the Reactions of Naphthalene, 2-Methylnaphthalene, and 2,3-Dimethylnaphthalene with OH Radicals and with O_3 at 295 ± 1 K. *Int. J. Chem. Kinet.* **1986**, *18*, 569−573.

(22) Sander, L. C.; Wise, S. A. In *NIST Chemistry WebBook*; NIST Standard Reference Database 69; National Institute of Standards and Technology: Gaithersburg, MD, (January) 2014, naphthalene (http://webbook.nist.gov).

(23) Brubaker, W. W.; Hites, R. A. OH Reaction Kinetics of Polycyclic Aromatic Hydrocarbons and Polychlorinated Dibenzo-*p*-Dioxins and Dibenzofurans. *J. Phys. Chem. A* **1998**, *102*, 915−921.

(24) Klöpffer, V. W.; Frank, R.; Kohl, E. G.; Haag, F. Quantitative Erfassung der Photochemischen Tansformationsprozesse in der Troposphare. *Chem. Ztg.* **1986**, *110*, 57−62.

(25) Atkinson, R. Kinetic and Mechanism of the Gas-Phase Reactions of the Hydroxyl Radical with Organic Compounds under Atmospheric Conditions. *Chem. Rev.* **1985**, *85*, 69−201.

(26) Ricca, A.; Bauschlicher, C. W., Jr. The Reactions of Polycyclic Aromatic Hydrocarbons with OH. *Chem. Phys. Lett.* **2000**, *328*, 396−402.

(27) Zhang, Z.; Lin, L.; Wang, L. Atmospheric Oxidation Mechanism of Naphthalene Initiated by OH Radical. A Theoretical Study. *Phys. Chem. Chem. Phys.* **2012**, *14*, 2645−2650.

(28) Hollman, D. S.; Simmonett, A. C.; Schaefer, H. F. The Benzene + OH Potential Energy Surface: Intermediates and Transition States. *Phys. Chem. Chem. Phys.* **2011**, *13*, 2214−2221.

(29) Zade, S. S.; Bendikov, M. Reactivity of Acenes: Mechanisms and Dependence on Acene Length. *J. Phys. Org. Chem.* **2012**, *25*, 452−461.

(30) Suresh, C. H.; Gadre, S. R. Clar's Aromatic Sextet Theory Revisited via Molecular Electrostatic Potential Topography. *J. Org. Chem.* **1999**, *64*, 2505−2512.

(31) Casasnovas, R.; Frau, J.; Ortega-castro, J.; Salva, A.; Donoso, J.; Munoz, F. Simplification of the CBS-QB3Method for Predicting Gas-Phase Deprotonation Free Energies. *Int. J. Quantum Chem.* **2010**, *110*, 323−330.

(32) Montgomery, J. A.; Frisch, M. J.; Ochterski, J. W.; Petersson, G. A. A Complete Basis Set Model Chemistry. VI. Use of Density Functional Geometries and Frequencies. *J. Chem. Phys.* **1999**, *110*, 2822−2827.

(33) Ochterski, J. W.; Petersson, G. A.; Montgomery, J. A. A Complete Basis Set Model Chemistry. V. Extensions to Six or More Heavy Atoms. *J. Chem. Phys.* **1996**, *104*, 2598−2619.

(34) Nyden, M. R.; Petersson, G. A. Complete Basis Set Correlation Energies. I. The Asymptotic Convergence of Pair Natural Orbital Expansions. *J. Chem. Phys.* **1981**, *75*, 1843−1862.

(35) Petersson, G. A.; Bennett, A.; Tensfeld, T. G.; Al-Laham, M. A.; Shirley, W.; Matzaris, J. A Complete Basis Set Model Chemistry. I. The Total Energies of Closed-Shell Atoms and Hydrides of the First-Row Elements. *J. Chem. Phys.* **1988**, *89*, 2193−2218.

(36) Petersson, G. A.; Al-Laham, M. A. A Complete Basis Set Model Chemistry. II. Open-Shell Systems and the Total Energies of the First-Row Atoms. *J. Chem. Phys.* **1991**, *94*, 6081−6090.

(37) Petersson, G. A.; Yee, A. K.; Bennett, A. Complete Basis Set Correlation Energies. III. The Total Correlation Energy of the Neon Atom. *J. Chem. Phys.* **1983**, *83*, 5105−5128.

(38) Montgomery, J. A.; Ochterski, J. W.; Petersson, G. A. A Complete Basis Set Model Chemistry. IV. An Improved Atomic Pair Natural Orbital Method. *J. Chem. Phys.* **1994**, *101*, 5900−5909.

(39) Montgomery, J. A.; Frisch, M. J.; Ochterski, J. W.; Petersson, G. A. A Complete Basis Set Model Chemistry. VII. Use of the Minimum Population Localization Method. *J. Chem. Phys.* **2000**, *112*, 6532−6542.

(40) Cysewski, P. An Ab Initio Study on Nucleic Acid Bases Aromaticities. *J. Mol. Struct. (THEOCHEM)* **2005**, *714*, 29−34.

(41) Schleyer, P. v. R.; Maerker, C.; Dransfeld, A.; Jiao, H.; van Eikema Hommes, N. J. R. Nucleus-Independent Chemical Shifts: A Simple and Efficient Aromaticity Probe. *J. Am. Chem. Soc.* **1996**, *118*, 6317−6318.

(42) Nigam, S.; Majumder, C.; Kulshreshtha, S. K. Theoretical Study of Aromaticity in Inorganic Tetramer Clusters. *J. Chem. Sci.* **2006**, *118*, 575−578.

(43) Schleyer, P. v. R.; Manoharan, M.; Wang, Z. X.; Kiran, B.; Jiao, H. J.; Puchta, R.; Hommes, N. Dissected Nucleus-Independent Chemical Shift Analysis of π-Aromaticity and Antiaromaticity. *Org. Lett.* **2001**, *3*, 2465−2468.

(44) Schleyer, P. v. R.; Jiao, H.; Goldfuss, B.; Freeman, P. K. Aromaticity and Antiaromaticity in Five-Membered C_4H_4X Ring Systems: "Classical" and "Magnetic" Concepts May Not Be "Orthogonal. *Angew. Chem., Int. Ed. Engl.* **1995**, *34*, 337−340.

(45) Reed, A. E.; Weinstock, R. B.; Weinhold, F. Natural Population Analysis. *J. Chem. Phys.* **1985**, *83*, 735−746.

(46) Badenhoop, J. K.; Weinhold, F. Natural Steric Analysis of Internal Rotation Barriers. *Int. J. Quantum Chem.* **1999**, *72*, 269−280.

(47) Frisch, M. J. ; Trucks, G. W.; Schlegel, H. B.; Scuseria, G. E.; Robb, M. A.; Cheeseman, J. R.; Scalmani, G.; Barone, V.; Mennucci, B.; Petersson, G. A.; et al. *Gaussian 09*, Revision B.01; Gaussian: Wallingford, CT, 2009.

(48) Dennington, I. I. R.; Keith, T.; Millam, J.; Eppinnett, K.; Hovell, W. L.; Gilliland, R. *GaussView*, Version 3.09; Semichem, Inc.: Shawnee Mission, KS, 2003.

(49) Raghavachari, K.; Trucks, G. W.; Pople, J. A.; Head-Gordon, M. A Fifth-Order Perturbation Comparison of Electron Correlation Theories. *Chem. Phys. Lett.* **1989**, *157*, 479−483.

(50) Bartlett, R. J.; Watts, J. D.; Kucharski, S. A.; Noga, J. Non-Iterative Fifth-Order Triple and Quadruple Excitation Energy Corrections in Correlated Methods. *Chem. Phys. Lett.* **1990**, *165*, 513−522.

(51) Stanton, J. F. Why CCSD(T) Works: A Different Perspective. *Chem. Phys. Lett.* **1997**, *281*, 130−134.

(52) Szabo, A.; Ostlund, N. S. *Modern Quantum Chemistry: Introduction to Advanced Electronic Structure Theory*; McGraw-Hill: New York, 1989.

(53) Lee, C.; Yang, W.; Parr, R. G. Development of the Colle-Salvetti Correlation-Energy Formula into a Functional of the Electron Density. *Phys. Rev. B* **1988**, *37*, 785−789.

(54) Becke, A. D. Density-Functional Thermochemistry. III. The Role of Exact Exchange. *J. Chem. Phys.* **1993**, *98*, 5648−5652.

(55) Sousa, J. A.; Silva, P. P.; Machado, A. E. H.; Reis, M. H. M.; Romanielo, L. L.; Hori, C. E. Application of Computational Chemistry Methods to Obtain Thermodynamic Data for Hydrogen Production From Liquefied Petroleum Gas. *Braz. J. Chem. Eng.* **2013**, *30*, 83−93.

(56) Ess, D. H. Quantum Mechanical Theory of Reactivity and Selectivity in Organic and Organometallic Reactions. *Ph.D. Dissertation*, University of California, Los Angeles, 2007.

(57) Chai, J. D.; Head-Gordon, M. Long-Range Corrected Hybrid Density Functionals with Damped Atom-Atom Dispersion Corrections. *Phys. Chem. Chem. Phys.* **2008**, *10*, 6615−6620.

(58) Zhao, Y.; Truhlar, D. G. Density Functionals with Broad Applicability in Chemistry. *Acc. Chem. Res.* **2008**, *41*, 157−167.

(59) Dunning, T. H. Gaussian Basis Sets for Use in Correlated Molecular Calculations. I. The Atoms Boron through Neon and Hydrogen. *J. Chem. Phys.* **1989**, *90*, 1007−1023.

(60) McQuarrie, D. A. *Statistical Mechanics*; Harper and Row: New York, 1976.

(61) Herzberg, G. H. *Molecular Spectra and Molecular Structure. II Infrared and Raman Spectra of Polyatomic Molecules*; Van Nostrand Reinhold: New York, 1945.

(62) Canneaux, S.; Vandeputte, R.; Hammaecher, C.; Louis, F.; Ribaucour, M. Thermochemical Data and Additivity Group Values for Ten Species of *O*-Xylene Low-Temperature Oxidation Mechanism. *J. Phys. Chem. A* **2012**, *116*, 592−610.

(63) Fukui, F. A Formulation of the Reaction Coordinate. *J. Phys. Chem.* **1970**, *74*, 4161−4163.

(64) McIver, J. W., Jr. Structure of Transition States. Are They Symmetric? *Acc. Chem. Res.* **1974**, *7*, 72−77.

(65) Tokmakov, I. V.; Lin, M. C. Kinetics and Mechanism of the OH + C_6H_6 Reaction: A Detailed Analysis with First-Principles Calculations. *J. Phys. Chem. A* **2002**, *106*, 11309−11326.

(66) Boys, S. F.; Bernardi, F. Calculation of Small Molecular Interactions by Differences of Separate Total Energies-Some Procedures with Reduced Errors. *Mol. Phys.* **1970**, *19*, 553−566.

(67) Huang, M.; Wang, Z.; Yang, Y.; HAO, L.; Zhao, W.; Gao, X.; Fang, L.; Zhang, W. Intramolecular Hydrogen Bond in the Hydroxycyclohexadienyl Peroxy Radicals. *Int. J. Quantum Chem.* **2007**, *107*, 1092−1098.

(68) Walczak, K.; Friedrich, J.; Dolg, M. On the Incremental Evaluation of BSSE-Free Interaction Energies. *Chem. Phys.* **2009**, *365*, 38−43.

(69) Chang, R. *Physical Chemistry for the Biosciences*; University Science Books: Sausalito, CA, 2005.

(70) Moore, J. W.; Pearson, R. G. *Kinetics and Mechanism-The Study of Homogeneous Chemical Reactions*, 3rd ed.; Wiley: New York, 1981.

(71) Carstensen, H. H.; Dean, A. M.; Deutschmann, O. Rate Constants for the H Abstraction from Alkanes (R−H) by R′O_2 Radicals: A Systematic Study on the Impact of R and R′. *Proc. Combust. Inst.* **2007**, *31*, 149−157.

(72) Duncan, W. T.; Bell, R. L.; Truong, T. N. TheRate: Program for Ab Initio Direct Dynamics Calculations of Thermal and Vibrational-State-Selected Rate Constants. *J. Comput. Chem.* **1998**, *19*, 1039−1052.

(73) Varma, D. H.; Raghunath, P.; Lin, M. C. Ab Initio Chemical Kinetics for the Reaction of an H Atom with Si_3H_8. *J. Phys. Chem. A* **2010**, *114*, 3642−3648.

(74) Wu, S. Y.; Raghunath, P.; Wu, J. S.; Lin, M. C. Ab Initio Chemical Kinetic Study for Reactions of H Atoms with SiH_4 and Si_2H_6: Comparison of Theory and Experiment. *J. Phys. Chem. A* **2010**, *114*, 633−639.

(75) Gilbert, R. G.; Smith, S. C. *Theory of Unimolecular and Recombination Reactions*; Blackwell Scientific Publications: Oxford, U.K, 1990.

(76) Rao, H. B.; Zeng, X. Y.; He, H.; Li, Z. R. Theoretical Investigations on Removal Reactions of Ethenol by H Atom. *J. Phys. Chem. A* **2011**, *115*, 1602−1608.

(77) Robinson, P. J.; Holbrook, K. A. *Unimolecular Reactions*; Wiley: New York, 1972.

(78) Steinfeld, J. I.; Francisco, J. S.; Hase, W. L. *Chemical Kinetics and Dynamics*; Prentice- Hall: Englewood Cliffs, NJ, 1999.

(79) Eyring, H.; Lin, S. H.; Lin, S. M. *Basic Chemical Kinetics*; Wiley: New York, 1980.

(80) Canneaux, S.; Bohr, F.; Henon, E. KiSThelP: A Program to Predict Thermodynamic Properties and Rate Constants from Quantum Chemistry Results. *J. Comput. Chem.* **2014**, *35*, 82−93.

(81) Troe, J. Theory of Thermal Unimolecular Reactions at Low Pressures. II. Strong Collision Rate Constants: Applications. *J. Chem. Phys.* **1977**, *66*, 4758−4775.

(82) Hirschfelder, J. O.; Curtiss, C. F.; Bird, R. B. *Molecular Theory of Gases and Liquids*; Wiley: New York, 1954.

(83) Iwai, Y.; Higashi, H.; Uchida, H.; Arai, Y. Molecular Dynamics Simulation of Diffusion Coefficients of Naphthalene and 2-Naphthol in Supercritical Carbon Dioxide. *Fluid Phase Equilib.* **1997**, *127*, 251−261.

(84) Singleton, D. L.; Cvetanovic, R. J. Temperature Dependence of the Reaction of Oxygen Atoms with Olefins. *J. Am. Chem. Soc.* **1976**, *98*, 6812−6819.

(85) Alvarez-Idaboy, J. R.; Galano, A. Counterpoise Corrected Interaction Energies are not Systematically Better than Uncorrected ones: Comparison with CCSD(T) CBS Extrapolated Values. *Theor. Chem. Acc.* **2010**, *126*, 75−85.

(86) Sheng, X. W.; Mentel, L.; Gritsenko, O. V.; Baerends, E. J. Counterpoise Correction is Not Useful for Short and Van der Waals Distances but May Be Useful at Long Range. *J. Comput. Chem.* **2011**, *32*, 2896−2901.

(87) Leffler, J. E. Parameters for the Description of Transition States. *Science* **1953**, *117*, 340−341.

(88) Agmon, N.; Levine, R. D. Energy, Entropy and the Reaction Coordinate: Thermodynamic-Like Relations in Chemical Kinetics. *Chem. Phys. Lett.* **1977**, *52*, 197−201.

(89) Chen, W.; Schlegel, H. B. Evaluation of S^2 for Correlated Wave-Functions and Spin Projection of Unrestricted M?ller-Plesset Perturbation Theory. *J. Chem. Phys.* **1994**, *101*, 5957−5968.

(90) Stanton, J. F. On the Extent of Spin Contamination in Open-Shell Coupled-Cluster Wave Functions. *J. Chem. Phys.* **1994**, *101*, 371−374.

(91) Cederbaum, L. S.; Tarantelli, F.; P Winkler, P. Non-analyticity of self-consistent field approaches: failure of predicting symmetry. *J. Phys. B: At. Mol. Opt. Phys.* **1990**, *23*, L747−L752.

(92) Cederbaum, L. S.; Winkler, P. Dilatation Transformation and Sum Rules for General Potentials Including Self-Consistent Field Potentials. *Theor. Chim. Acta.* **1994**, *88*, 257−270.

(93) Hajgató, B.; Szieberth, D.; Geerlings, P.; De Proft, F.; Deleuze, M. S. A Benchmark Theoretical Study of the Electronic Ground State and of the Singlet-Triplet Split of Benzene and Linear Acenes. *J. Chem. Phys.* **2009**, *131*, 224321−224338.

(94) Huzak, M.; Hajgató, B.; Deleuze, M. S. Half-Metallicity and Spin-Contamination of the Electronic Ground State of Graphene Nanoribbons and Related Systems: an Impossible Compromise? *J. Chem. Phys.* **2011**, *135*, 104704−104722.

(95) Hajgató, B.; Deleuze, M. S. Quenching of Magnetism in Hexagonal Graphene Nanoflakes by Non-Local Electron Correlation. *Chem. Phys. Lett.* **2012**, *553*, 6−10.

(96) Deleuze, M. S.; Huzak, M.; Hajgató, B. Half-Metallicity of Graphene Nanoribbons and Related Systems: a New Quantum Mechanical El Dorado for Nanotechnologies··· or a Hype for Materials Scientists? *J. Mol. Mod.* **2013**, *19*, 2699−2714.

(97) Deleuze, M. S.; Claes, L.; Kryachko, E. S.; François, J. P. Benchmark Theoretical Study of the Ionization Threshold of Benzene and Oligoacenes. *J. Chem. Phys.* **2003**, *119*, 3106−3119.

(98) Hajgató, B.; Deleuze, M. S.; Tozer, D. J.; De Proft, F. A Benchmark Theoretical Study of the Electron Affinities of Benzene and Linear Acenes. *J. Chem. Phys.* **2008**, *129*, 84308−84322.

(99) Glowacki, D. R.; Liang, C. H.; Morley, C.; Pilling, M. J.; Robertson, S. H. MESMER: An Open-Source Master Equation Solver for Multi-Energy Well Reactions. *J. Phys. Chem. A* **2012**, *116*, 9545−9560.

(100) Lendvay, G. Bond Orders from Ab Initio Calculations and a Test of the Principle of Bond Order Conservation. *J. Phys. Chem.* **1989**, *93*, 4422−4429.

(101) Reed, A. E.; Curtiss, L. A.; Weinhold, F. Intermolecular Interactions from a Natural Bond Orbital, Donor-Acceptor Viewpoint. *Chem. Rev.* **1988**, *88*, 899−926.

(102) Moyano, A.; Periclas, M. A.; Valenti, E. A Theoretical Study on the Mechanism of the Thermal and the Acid-Catalyzed Decarboxylation of 2-Oxetanones (*β*-Lactones). *J. Org. Chem.* **1989**, *54*, 573−582.

(103) Carpenter, J. E.; Weinhold, F. Analysis of the Geometry of the Hydroxymethyl Radical by the "Different Hybrids for Different Spins"

Natural Bond Orbital Procedure. *J. Mol. Struct. (THEOCHEM)* **1988**, *169*, 41−62.

(104) Shiroudi, A.; Deleuze, M. S. Theoretical Study of the Oxidation Mechanisms of Naphthalene Initiated by Hydroxyl Radicals: The H Abstraction Pathway. *J. Phys. Chem. A* **2014**, *118*, 3625−3636.